Available online at www.sciencedirect.com

ScienceDirect

Geochimica et Cosmochimica Acta 236 (2018) 79–98

Geochimica et Cosmochimica Acta

www.elsevier.com/locate/gca

Trace element (Mn, Zn, Ni, V) and authigenic uranium (aU) geochemistry reveal sedimentary redox history on the Juan de Fuca Ridge, North Pacific Ocean

Kassandra M. Costa [a,b,*], Robert F. Anderson [a,b], Jerry F. McManus [a,b], Gisela Winckler [a,b], Jennifer L. Middleton [a], Charles H. Langmuir [c]

[a] Lamont-Doherty Earth Observatory of Columbia University, Palisades, NY 10964, USA
[b] Department of Earth and Environmental Sciences, Columbia University, New York, NY 10027, USA
[c] Department of Earth and Planetary Sciences, Harvard University, Cambridge, MA 02138, USA

Received 15 August 2017; accepted in revised form 6 February 2018; available online 13 February 2018

Abstract

Changes in meridional overturning circulation and water mass chemistry can be recorded by oxygen concentrations in the deep ocean. Because the deep Pacific is the largest ocean reservoir, its oxygen concentrations may be related to global climate change. In this study, oxygen conditions in the past are reconstructed by contrasting the sedimentary geochemistry of multiple redox-sensitive trace elements (Mn, Ni, Zn, V corrected for terrigenous and hydrothermal inputs) and authigenic U (aU) from six sediment cores on the Juan de Fuca Ridge from 2.7-2.8 km depth. We find that Mn and Ni are indicators for oxygen-rich conditions, while Zn, V, and aU are indicators for oxygen-poor conditions. Relative Redox Potentials (RRPs) for each core are calculated by converting excess metal fluxes into binary presence/absence designations, weighting each element by the strength and direction of its redox indication, summing the five elements, and then averaging the data in 5kyr bins. Metal depositional histories from all six cores demonstrate low oxygen conditions during interglacial periods, particularly during 100–120 ka (MIS5) but also 200–250 ka (MIS7), and high oxygen conditions during glacial periods (MIS2-4 and MIS6). This redox pattern does not appear to be driven by organic matter flux to the sediment, as reconstructed by three different paleoproductivity proxies (organic carbon, opal, and excess barium). Instead higher oxygen concentrations on the Juan de Fuca Ridge may be a result of better ventilation during glacial periods, possibly due to enhanced North Pacific Intermediate Water formation. Alternatively, sedimentary redox conditions on the Juan de Fuca Ridge may be locally controlled by the deposition of hydrothermal sulfides from nearby vent fields.

Keywords: Authigenic uranium; Redox; Sediment geochemistry

1. INTRODUCTION

Oxygen concentrations in the deep ocean are an important indicator of global climate conditions. While today oxygen persists in deepwaters due to the continuous irrigation of more recently ventilated water, changes in circulation geometry in the past could have displaced this supply pipeline. Reduced ventilation limits the starting oxygen concentrations, but biological processes are largely responsible for the magnitude of subsequent oxygen depletion as the water mass transits at depth. The coupling of carbon and oxygen in respiration may therefore cause oxygen

* Corresponding author at: Lamont-Doherty Earth Observatory of Columbia University, Palisades, NY 10964, USA.
E-mail address: kcosta@ldeo.columbia.edu (K.M. Costa).

https://doi.org/10.1016/j.gca.2018.02.016
0016-7037/

depletion coincident with greater carbon storage. Reconstructions of paleo-redox conditions in the deep waters of the Pacific can help determine the water mass structure and chemistry that allowed the ocean to take up so much CO_2 during past glacial periods (Broecker, 1982; Sigman and Boyle, 2000).

Paleo-oxygen concentrations can be straightforward to interpret under the right conditions, such as when the onset of anoxic conditions suffocates benthic organisms and allows the development and preservation of fine sedimentary laminations (Crusius et al., 2004; Davies et al., 2011). But where low sedimentation rates limit the record of laminations, oxygen concentrations in the past can be reconstructed by contrasting the sedimentary geochemistry of multiple redox-sensitive trace elements (Elderfield, 1985). Various combinations of V, Mo, U, Re, Cd, Mn, Cu, and Fe have been employed to reconstruct redox conditions across the global ocean, including the Cariaco Basin (Yarincik et al., 2000), the California Margin (McManus et al., 2005; Shimmield and Price, 1986), and the eastern margin of North America (Morford et al., 2009), amongst many others. Beyond the coastal margins, sedimentary environments near mid-ocean ridges have proven advantageous to paleo-redox studies of deepwaters because hydrothermal activity increases redox-sensitive trace element concentrations that offer stronger indications of past changes in sedimentary redox conditions than can be extracted from sediments elsewhere (Mills et al., 2010; Schaller et al., 2000).

In this study, we use sedimentary concentrations of trace metals (Mn, Ni, Zn, V) and authigenic U (aU) to reconstruct redox conditions over the past 250kyr on the Juan de Fuca Ridge. The antiphased chemistry of aU and Mn anchor calculations of relative redox potential (RRP), which records the relative changes in sedimentary redox conditions based on the presence or absence of aU, Mn, Ni, Zn, and V. Because sedimentary redox records integrate changes in bottom water oxygen with the local flux of reductants (electron donors), the variability in organic matter and hydrothermal sulfide deposition must be considered before variability in RRP can be interpreted as changes in ventilation. We present new records of organic carbon, excess barium, and opal fluxes to constrain the variability in paleoproductivity and burial of organic matter in this region. We also compare the RRP with previously published records of hydrothermal activity along the ridge to investigate whether sulfide deposition may be influencing the redox history of North Pacific sediments.

2. METHODS

2.1. Core sites and stratigraphy

Samples were taken from six cores on the Juan de Fuca Ridge (Fig. 1) collected on the SeaVOICE cruise (AT26-19) of the R/V Atlantis in September 2014. Cores were retrieved in two E-W transects in a semi-grid on the western flanks of the ridge and targeted on ridge-parallel crests (2655–2794 m) to maximize carbonate preservation (Costa et al., 2016). The average spacing between cores is about 20 km. Age models for the JdFR cores are well-constrained based on radiocarbon dates, benthic $\delta^{18}O$, and stratigraphically tuned density cycles (Costa et al., 2016). Dry bulk density and coarse fraction >63 μm (Costa et al., 2016), as well as bulk particle flux (Costa and McManus, 2017) all show distinct glacial-interglacial cycles, with high-density, coarse sediment characterizing glacial deposition.

2.2. Uranium analyses

Samples ($n = 1097$) were analyzed for uranium (^{238}U, ^{235}U, ^{234}U) by isotope dilution inductively coupled plasma mass spectrometry (ICP-MS) following the procedure described by Costa and McManus (2017). Samples (100 mg) were randomized and spiked with ^{236}U and ^{229}Th before processing with complete acid digestion and column chromatography (Fleisher and Anderson, 2003). Isotopes were measured on an Element 2 ICP-MS at Lamont-Doherty Earth Observatory (LDEO) of Columbia University. Discrete sediment aliquots ($n = 106$) of an internal sediment standard (VOICE Internal MegaStandard, VIMS) were processed and analyzed for quality control. The VIMS replicates indicate that the analytical procedure and measurement are externally reproducible within 6.2% on ^{238}U and 3.7% on ^{232}Th (Costa and McManus, 2017). The lithogenic fraction of uranium was calculated using a detrital $^{238}U/^{232}Th$ activity ratio of 0.48 (Costa and McManus, 2017), the value which $^{238}U/^{232}Th$ reaches as the ^{232}Th concentration approaches the average lithogenic value (10.7 ppm, Taylor and McLennan, 1995) and similar to other lithogenic $^{238}U/^{232}Th$ values from elsewhere in the North Pacific: 0.5 ± 0.1 (Serno et al., 2015) and 0.53 (Taguchi and Narita, 1995). Subtracting the lithogenic uranium from the total uranium concentration determines the concentration of authigenic uranium (aU). aU fluxes are calculated using age model based mass accumulation rates (MAR) derived from the dry bulk density and linear sedimentation rates (Costa et al., 2016). MAR include both the particle rain rate through the water column as well as the lateral particle contributions due to sediment focusing (or winnowing). The total sedimentation rates influence sedimentary aU precipitation because they control the diffusion depth of dissolved U(VI) from overlying bottom waters through pore waters to the redox boundary where reduction to U (IV) occurs (Anderson, 1982; Anderson et al., 1989b; Barnes and Cochran, 1990; Klinkhammer and Palmer, 1991). The in situ precipitation of sedimentary aU means that the total (age model-based) MAR is the appropriate parameter to use when evaluating the diffusive flux of U into the sediments. Constant flux proxies, like ^{230}Th, specifically reconstruct the particle rain through the water column and thus are not relevant to formation of authigenic metals within the sediment.

2.3. Trace element concentrations

Intensities (count rates) of V, Ni, Zn, Fe, Mn, Ba, and Ti were measured with an X-ray fluorescence (XRF) core scanner (ITRAX, Cox Ltd., Sweden) at Lamont-Doherty

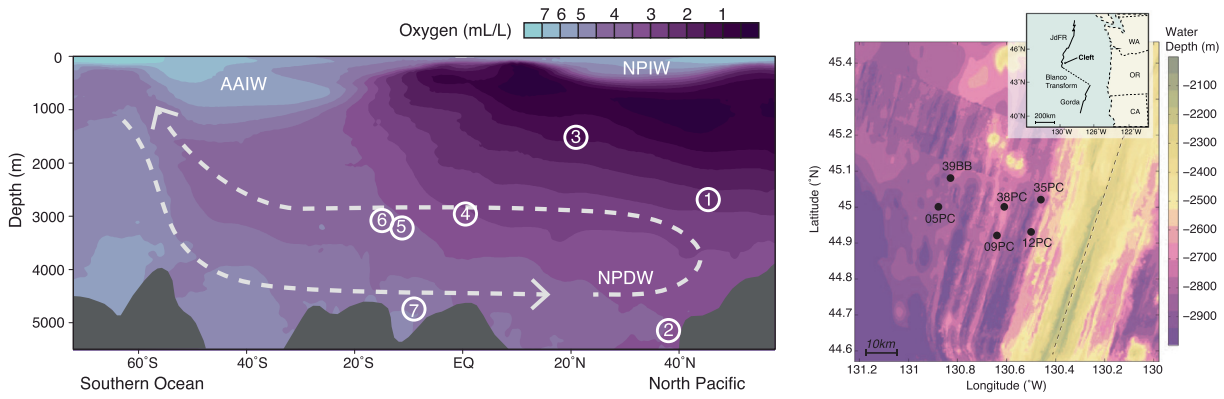

Fig. 1. (*Left*) Longitudinal section of oxygen concentrations from a 500 km swath along 140°W (Garcia et al., 2014). Dashed arrows show general Pacific meridional overturning circulation. Water masses are labeled as NPDW (North Pacific Deep Water), AAIW (Antarctic Intermediate Water), and NPIW (North Pacific Intermediate Water). Core locations referred to in this study have been zonally projected onto the oxygen section (white circles). 1. AT26-19 set of 6 cores (this study) 2. SO202-1-39-3 (Korff et al., 2016) 3. 72DK-9 (Mangini et al., 1990) 4. ML1208-17PC (Jacobel et al., 2017) 5. Y-71-7-53P (Lund et al., 2016; Schaller et al., 2000) 6. GS7202-35 (Mills et al., 2010) 7. VA13-2 (Mangini et al., 1990). (*Right*) Bathymetric map of the Cleft Segment, with inset showing the geographic position of the Juan de Fuca Ridge in the Northeast Pacific Ocean. The ridge can be identified as the NE-SW trending bathymetric high (in yellow), and the axis is identified with a dashed line. AT26-19 core locations on the western flanks of the ridge are shown with black dots (Costa et al., 2017c). (For interpretation of the references to colour in this figure legend, the reader is referred to the web version of this article.)

Earth Observatory of Columbia University (LDEO). Split core surfaces were smoothed and covered with ChemPlex Proline transmission film to minimize desiccation during analysis. XRF was performed at 2 mm resolution, using an integration time of 2 s and a molybdenum X-ray source set to 30 kV and 45 mA. XRF intensities were calibrated using discrete measurements analyzed by flux fusion as previously described in Costa et al. (2017c). Samples from 05PC, 09PC, and 12PC were selected to cover the full range of XRF intensities observed in each core, and elemental concentrations were analyzed by flux fusion following the procedure of Murray et al. (2000). Dried, homogenized samples (100 ± 5 mg) were combined with lithium metaborate flux (400 ± 10 mg) in graphite crucibles and fused at 1050 °C for 8–10 min. The graphite crucibles were removed from the furnace and agitated to ensure aggregation of the fused material. After reheating to 1050 °C, the fused bead was dissolved in 10% HNO_3, agitated for approximately 10 min, and then filtered and diluted for analysis. Samples were analyzed on an Agilent 720 Inductively Coupled Plasma Optical Emission Spectrometer (ICP-OES) at LDEO, and ICP-OES intensity data were calibrated to concentrations with fluxed standard reference materials (JLS-1, JDO-1, SCO-1, AGV-2, JB1-a, W-2a, BCR, BHVO-2 Supplementary Fig. S1). Empirical calibrations of the XRF data were generated by least squares linear regression of the XRF intensities and discrete elemental data. The XRF records were smoothed at 1 cm scale and interpolated onto the depths of the discrete samples. Overall the ICP data provide robust calibrations for the high-resolution XRF records (Fig. 2). As no inter-core discrepancies were apparent, the same calibration was applied to all six cores. Calibrations for Mn ($r^2 = 0.87$), Fe ($r^2 = 0.92$), and Ti ($r^2 = 0.86$) were previously published (Costa et al., 2017c).

Total metal concentrations (V, Ni, Zn, Mn, Fe) in pelagic sediment may be governed by several different processes, including variations in hydrothermal activity and lithogenic inputs in addition to redox conditions. It is therefore necessary to quantitatively account for the lithogenic and hydrothermal variability of each metal before interpreting the redox signals. Ti is almost entirely derived from the lithogenic fraction (Murray et al., 1993), in contrast to Al, which can be enriched in hydrothermal fluids (Elderfield et al., 1993; Lunel et al., 1990; Resing et al., 2015; Von Damm et al., 1985). Multiplying Ti by the average ratio of upper continental crust (e.g., Fe/Ti of 11.7wt%/wt%, Taylor and McLennan, 1995) constrains the lithogenic metal contributions. Additional discussion of lithogenic endmembers is provided in Costa et al. (2017c). Despite the potential hydrothermal effects on Al, Al/Ti ratios vary by only ~2% throughout the interval of interest (Supplementary Data Table S2), which would be consistent with relatively stable lithogenic endmembers.

Once the lithogenic metal concentration is subtracted from the total metal concentration, the residual metal concentration varies both in terms of hydrothermal activity and diagenesis. Because iron is the major component of hydrothermal particulates (Edmonds and German, 2004; Feely et al., 1994, 1987), scaling the non-lithogenic Fe record by average metal/Fe ratios within the hydrothermal plume will approximate the variability in hydrothermal metal inputs over time. Hydrothermal ratios (75th percentile) for Mn/Fe (0.0174 wt%/wt%), V/Fe (28.2 ppm/wt%), and Zn/Fe (32.7 ppm/wt%) were measured in hydrothermal particulates from the Cleft Segment at the Juan de Fuca Ridge (Feely et al., 1994). Ni/Fe ratios were not reported. Because hydrothermal V/Fe and Zn/Fe are relatively similar in value, we assume that hydrothermal Ni/Fe will behave comparably and assign it a value of 30

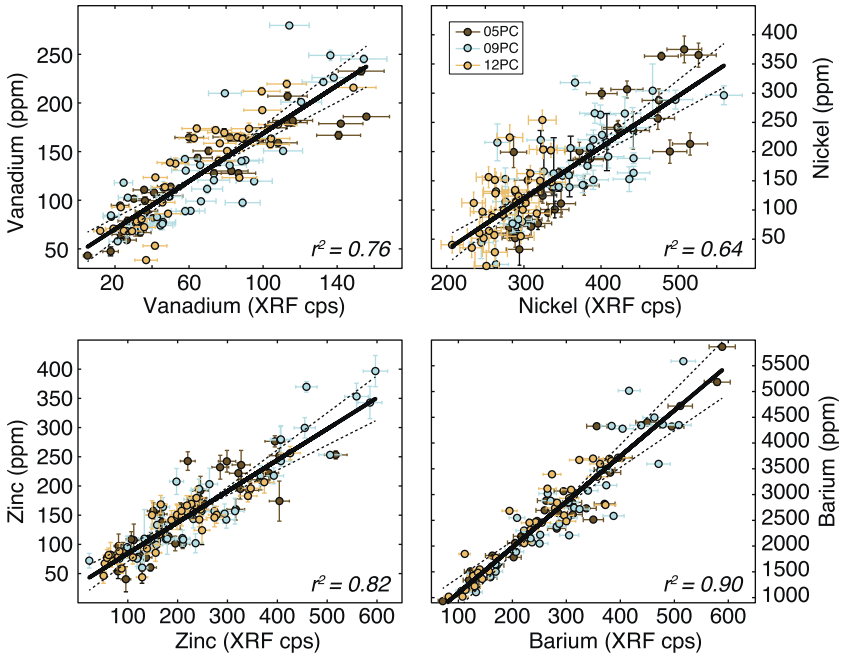

Fig. 2. Calibration of XRF scan data from counts per second (cps) to mass concentration (ppm) was determined by analyzing discrete sediment samples by flux fusion and ICP-OES. Pearson's correlation coefficients (r^2) are indicated for each element, all at $p < 0.001$. Agreement amongst the three cores (05PC, 09PC, and 12PC) analyzed by discrete analysis justifies the use of a single calibration curve for all six cores analyzed by XRF (05PC, 09PC, 12PC, 35PC, 38PC, 39BB). Error bars are 2σ, not shown when smaller than symbols. Calibrations for Mn ($r^2 = 0.87$), Fe ($r^2 = 0.92$), and Ti ($r^2 = 0.86$) have been previously published (Costa et al., 2017c).

ppm/wt%. This assumption is not unreasonable given that the hydrothermal correction is insensitive to variability in the metal/Fe ratios within the range of 10–50 ppm/wt% (Supplementary Fig. S2).

Subtracting the hydrothermal metal component from the non-lithogenic metal component leaves the residual excess metal (M_{xs}) interpreted here as the redistributed metal content in response to changing redox conditions within the sediment. As in aU fluxes, excess metal fluxes are calculated using age-model based mass accumulation rates derived from the dry bulk density and linear sedimentation rates (Costa et al., 2016)

In summary

$$M_{xs}flux = \left(M_{total} - Ti * \left(\frac{M}{Ti}\right)_{Lith} - Fe_H \left(\frac{M}{Fe}\right)_{Hydrothermal} \right) * \rho * LSR$$

where M is V, Ni, Mn, or Zn, ρ is the dry bulk density, and LSR is the linear sedimentation rate.

2.4. Paleo-productivity proxies

Biogenic opal was measured by alkaline extraction (Mortlock and Froelich, 1989) at LDEO. Samples were acidified with dilute hydrochloric acid and then oxidized with stabilized hydrogen peroxide. The residual sediment was then extracted in 2 N sodium carbonate for five hours at 80 °C. A silico-molybdate photoindicator was added to the leachates, and absorbance intensities at 812 μm were analyzed on a spectrophotometer. Total replicates (n = 6) of VIMS indicate that the analytical procedure and measurement are reproducible within ±6.7%.

Organic carbon concentrations were analyzed by combustion on an Element Analyzer at LDEO. Samples were acidified with dilute hydrochloric acid and then rinsed with deionized water till neutral pH was achieved. The residual non-carbonate fraction was freeze-dried and loaded in tin capsules. Because this analytical procedure has a poor yield (50% or less), the absolute organic carbon values may not be accurate and should not be employed in, e.g., direct comparisons with other published organic carbon records. Fortunately, reproducibility within ± 6% on total replicates (n = 5) of VIMS allows confidence in the temporal trends and relative variability, as the data are interpreted in this study.

Barium concentrations were measured by XRF and ICP-OES as detailed in Section 2.3. Excess barium (Ba_{xs}) was calculated by subtracting the lithogenic barium inputs using the Ti record and a lithogenic Ba/Ti ratio of 1833 ppm/wt% (Taylor and McLennan, 1995). Because these productivity proxies are delivered to the sediment in a vertical particle rain from the surface ocean, organic carbon, opal, and Ba_{xs} fluxes were calculated using ^{230}Th-normalized particle fluxes (Costa and McManus, 2017).

3. RESULTS

3.1. Authigenic uranium

Authigenic uranium (aU) is generally low (<1ppm) on the Juan de Fuca Ridge over the past 500 kyr (Fig. 3, Supplementary Table S1). This relatively constant background level is interrupted by peaks in aU that can reach as high as 5.3 ppm (Fig. 3A). Notably, high aU concentrations only occur in the two highest sedimentation rate

cores, 09PC and 35PC (Costa et al., 2016) (Fig. 3B), whereas the other four cores (05PC, 12PC, 38PC, 39BB) record nearly constant (low) aU concentrations over the past 500kyr. The highest aU concentrations in 35PC and 09PC occur during Marine Isotope Stage 5 (MIS5, 74–130 ka), but the two cores record different amplitudes and durations of the aU peak. In core 09PC, aU rises above background levels at 122 ka, peaks at 114 ka at 5.3 ppm, declines to a brief plateau at 109 ka at 2.8 ppm, and then returns to background aU levels (0.1 ppm) by ~90 ka. Thus, the high aU depositional period appears to last ~ 32kyr in 09PC. In core 35PC, aU rises above background levels at 121 ka, peaks at 111 ka at 4.3 ppm, where it remains until 88.8 ka when it starts gradually declining to background levels by 61 ka. Therefore, although the increase in aU concentrations in 35PC occurred at nearly the same time as in 09PC, the high aU depositional period lasted ~ 50 kyr, nearly twice as long and burying twice as much aU. Core 35PC also records peaks of aU of about ~ 2 ppm in the older interglacial period 199–237 ka (MIS7), which is not found in the other 5 cores. The earliest peak in aU in this core occurred during 272–306 ka (MIS8), and it is capped by the major turbidite event at 272 ka (Costa et al., 2016).

3.2. Trace Metals

3.2.1. Manganese

The redox-mobile fraction of manganese (Mn_{xs}) represents, on average, 74% of total manganese concentrations in the sediment (Supplementary Table S2). Mn_{xs} fluxes average 1.5–3.3 mg/cm^2 kyr in all cores except 09PC, where average Mn_{xs} fluxes are higher (5.0 mg/cm^2 kyr) and peak fluxes can reach as high as 35.7 mg/cm^2 kyr (Fig. 4). In general, Mn_{xs} fluxes are lower during interglacial periods than during glacial periods, and this cycling has the greatest range in the highest accumulation rate cores (09PC and 35PC). For example, in 09PC, Mn_{xs} fluxes average 1.9 mg/cm^2 kyr in MIS5 (100–120 ka) and 11.2 mg/cm^2 kyr in MIS2-4 (20–60 ka), a nearly tenfold increase in Mn_{xs} flux. Glacial-interglacial variability is damped in the oldest part of the core (>300 ka).

3.2.2. Nickel

The redox-mobile fraction of nickel (Ni_{xs}) represents, on average, 57% of total nickel concentrations in the sediment (Supplementary Table S2). Ni_{xs} fluxes average 24–118 μg/cm^2 kyr in all cores (Fig. 4). Peak fluxes reach as high as 625 μg/cm^2 kyr, and high frequency variability is particularly prominent in the high sedimentation rate cores (09PC, 35PC). Low sedimentation rate cores, notably 12PC and 38PC, record relatively constant Ni_{xs} deposition (e.g., −11 to 78 μg/cm^2 kyr in 12PC) compared to higher sedimentation rate cores (e.g., 7.7 to 625 μg/cm^2 kyr in 09PC). The Ni_{xs} and Mn_{xs} fluxes appear to be correlated over the last glacial cycle, with the highest correlation (r^2 = 0.67) of any two redox-sensitive elements (Fig. 5). From 150 to 250 ka, this relationship seems to reverse, with higher Mn_{xs} fluxes in MIS6 (150–200 ka) and MIS8 (250–300 ka), and higher Ni_{xs} fluxes in MIS7 (200–250 ka).

3.2.3. Zinc

The redox-mobile fraction of zinc (Zn_{xs}) represents, on average, 32% of total zinc concentrations in the sediment. Zn_{xs} fluxes average 20–83 μg/cm^2 kyr in all cores (Supplementary Table S2 and Fig. 4), with variability scaling with sedimentation rate as observed in Ni_{xs} fluxes. Peak fluxes reach as high as 354 μg/cm^2 kyr in 35PC, the core that also demonstrates the greatest dynamic range. Zn_{xs} fluxes are better correlated with aU fluxes (r^2 = 0.47) and Ni_{xs} fluxes (r^2 = 0.47) than with Mn_{xs} fluxes (r^2 = 0.17) (Fig. 5). High Zn_{xs} fluxes (greater than 120 μg/cm^2 kyr) occur during the last interglacial periods (MIS5), with several cores recording a peak at 110 ka. The duration of this high flux period scales with that of the aU fluxes, lasting the longest in 35PC (~50 kyr) and in 09PC (~30 kyr), with the other cores only recording a brief event. Zn_{xs} fluxes are also elevated in MIS7 in 35PC, peaking at 200 μg/cm^2 kyr at 214 ka, coincident with the high aU fluxes preserved in that core.

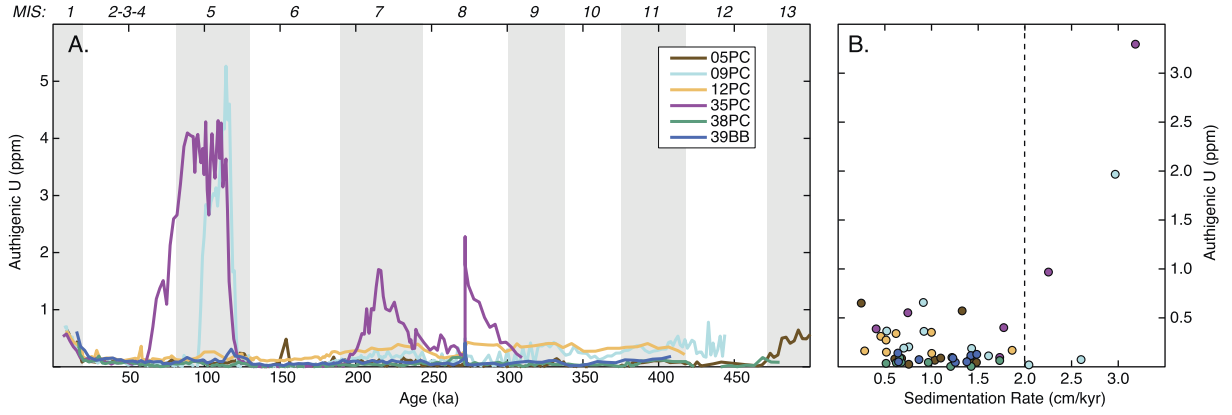

Fig. 3. Authigenic uranium (aU) records from the Juan de Fuca Ridge. (A) Peaks in aU occur during the last interglacial period in cores 09PC and 35PC, while the other cores show relatively constant and low aU burial over the entire 500kyr period. Interglacial periods are highlighted with gray bars. (B) aU concentrations vs. sedimentation rates, averaged over marine isotope stages (MIS). High aU concentrations are only preserved in the sedimentary record when sedimentation rates are greater than 2 cm/kyr (dashed line).

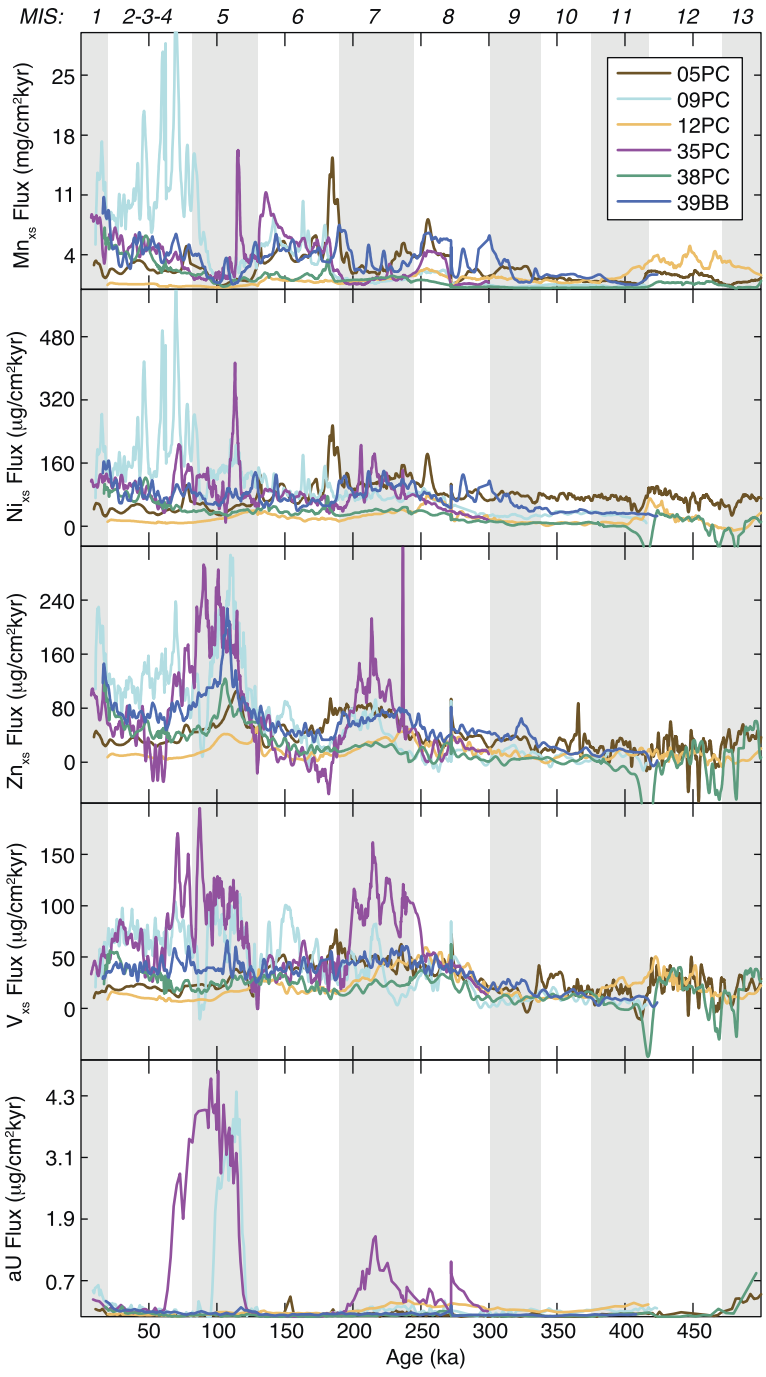

Fig. 4. Excess trace element fluxes over the past 500 kyr. Fluxes are calculated using age-model based mass accumulation rates. Mn_{xs} and Ni_{xs} fluxes are generally higher during glacial periods (MIS2-4 and MIS6) while Zn_{xs}, V_{xs}, and aU fluxes are higher during interglacial periods (MIS5 and MIS7). This variability is consistent with higher sediment oxygen concentrations during glacial periods and lower oxygen concentrations during interglacial periods. The presence of negative deposition rates, particularly in the oldest part of the record (>400 ka), may indicate (1) net loss of element from the sediment, presumably through diffusion to the water column, or (2) much lower hydrothermal metal/Fe ratios are present during that interval. Gray bars highlight interglacial periods, as identified by odd marine isotope stages (MIS).

3.2.4. Vanadium

The redox-mobile fraction of vanadium (V_{xs}) represents, on average, 32% of total vanadium concentrations in the sediment. V_{xs} fluxes average 22–70 µg/cm^2 kyr in all cores (Supplementary Table S2 and Fig. 4), and the overall lower fluxes lead to more similar depositional records from the high and low sedimentation rate cores. Peak fluxes reach as high as 195 µg/cm^2 kyr in 35PC, the core that also demonstrates the greatest dynamic range. V_{xs} fluxes are better correlated with aU fluxes ($r^2 = 0.34$), Zn_{xs} fluxes

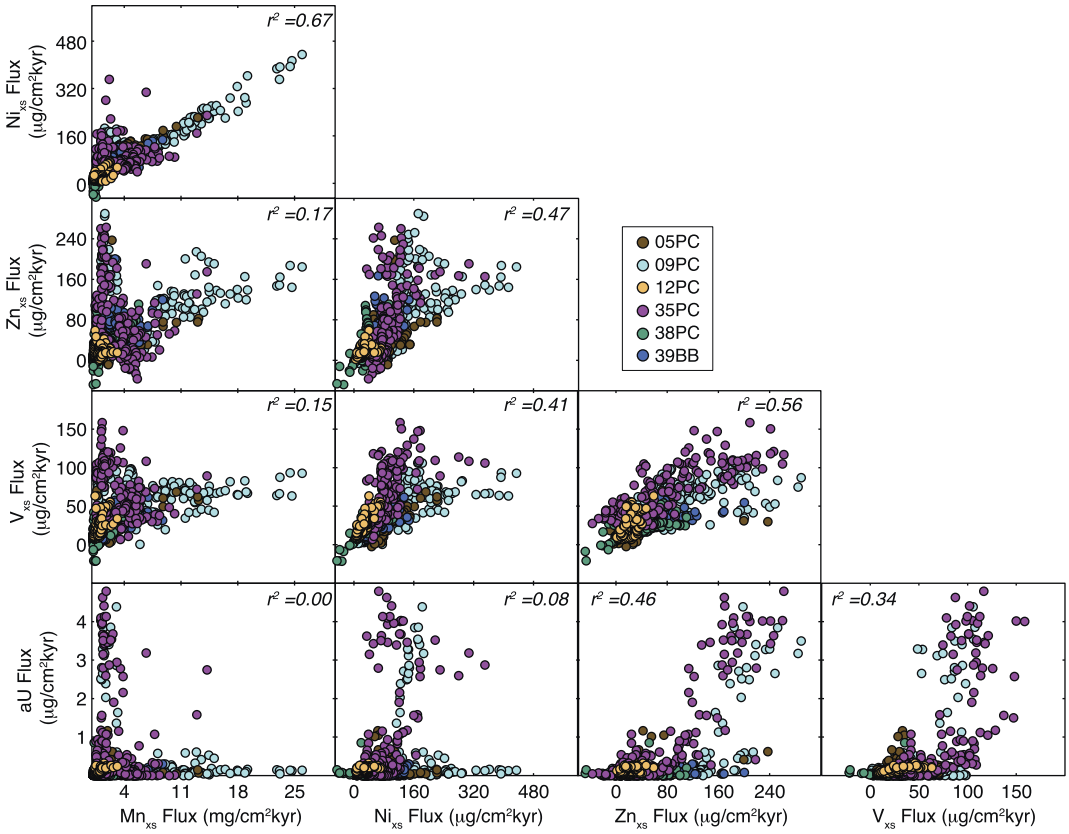

Fig. 5. Scatter plots showing relationships between Mn_{xs}, Ni_{xs}, Zn_{xs}, V_{xs}, and aU fluxes on the Juan de Fuca Ridge. Mn_{xs} and Ni_{xs} fluxes have the highest correlation ($r^2 = 0.67$), while Mn_{xs} and aU fluxes have no correlation at all ($r^2 = 0.00$). Zn_{xs} and V_{xs} fluxes are better correlated with aU fluxes than with Mn_{xs} fluxes. All correlations are at $p < 0.001$.

($r^2 = 0.56$), and Ni_{xs} fluxes ($r^2 = 0.41$) than with Mn_{xs} fluxes ($r^2 = 0.15$) (Fig. 5). High V_{xs} fluxes (greater than 80 µg/cm^2 kyr) occurred during oxygen poor interglacial periods (MIS5, MIS7) and low V_{xs} fluxes (below 60 µg/cm^2 kyr) occurred during oxygen rich glacial periods (MIS2-4, MIS6). High fluxes of V_{xs} during interglacial periods record a more square waveform than either aU or Zn_{xs}, which tend to peak in the middle of the oxygen poor interval.

3.3. Productivity

3.3.1. Organic Carbon

Organic carbon fluxes range from 2.2 to 8.9 mg/cm^2 kyr, but substantial scatter within the data suggests that a composite record may be more representative of the regional variability than that of any one individual core (Fig. 6). The data from the four cores examined were averaged (mean) within 5 kyr bins to create one regional record (black line, Fig. 6). Organic carbon fluxes are relatively low (less than 4 mg/cm^2 kyr) before 180 ka, but low resolution in this interval may alias higher frequency variability. From 180 ka onwards, the composite record demonstrates ~25 kyr cycles between relatively low organic carbon fluxes (4.3 mg/cm^2 kyr) and relatively higher organic carbon fluxes (5.9 mg/cm^2 kyr). The organic carbon flux peaks occur at 10, 35, 75, 100, 125, and 160 ka. Maximum organic

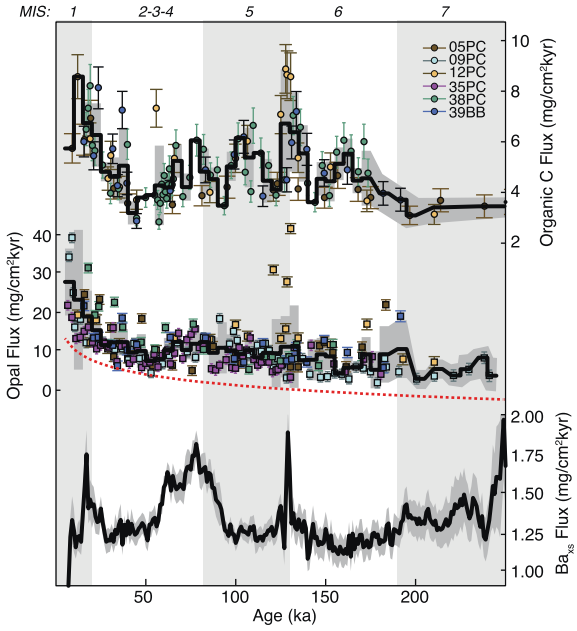

Fig. 6. Comparison of paleo-productivity records from the Juan de Fuca Ridge: organic carbon fluxes, opal fluxes, and Ba_{xs} fluxes. Gray bars highlight interglacial periods, as identified by odd marine isotope stages (MIS). One opal datapoint greater than 40 mg/cm^2 kyr is not shown (63 mg/cm^2 kyr at 12.4 ka).

carbon fluxes (greater than 8 mg/cm^2 kyr) occur just following the two glacial terminations, at 127 ka and 9.5 ka.

3.3.2. Opal

Fluxes of opal (biogenic silica), unlike organic carbon, are relatively consistent amongst the six different cores and show little to no temporal variability older than 50 ka (Fig. 6). Individual data hover between 5–15 mg/cm^2 kyr throughout the greater portion of the record, with the compiled data (binned as in the organic carbon fluxes) averaging around 10–11 mg/cm^2 kyr. The amplitude of orbital scale variability is quite muted, but some of the features in the opal flux record do align with those of the organic carbon record. During the early last interglacial (120–130 ka), several high opal flux values coincide with the slightly elevated organic carbon fluxes at that time. Opal fluxes increase from 110 ka (8.6 mg/cm^2 kyr) to local maxima at 80 ka and 65 ka (12.5–12.6 mg/cm^2 kyr) before reaching a minimum at 50 ka (7.9 mg/cm^2 kyr). After 50 ka, there is an upward trend in opal fluxes that reaches a maximum (23.7 mg/cm^2 kyr) in the early Holocene ~ 8.9 ka, approximately the top of the record. Overall, there appears to be a nearly exponential decay in opal flux from the most recent period (0–20 ka, 22 mg/cm^2 kyr) to the oldest part of the record (200–250 ka, 5.3 mg/cm^2 kyr).

3.3.3. Excess barium

Excess barium (Ba_{xs}) fluxes show a much more consistent pattern amongst the six different cores, which have been averaged (mean) in 1kyr bins to produce a single regional Ba_{xs} stack (Fig. 6). Background fluxes of Ba_{xs} are between 1.1 and 1.3 mg/cm^2 kyr, and this relatively constant baseline is punctured by only four prominent high flux features. Three are productivity spikes at 249 ka, 130 ka and 17 ka that occur during late deglaciation or early interglacial periods. The fourth feature is a broad productivity maximum that rises at 93 ka, peaks at 78 ka (1.8 mg/cm^2 kyr), and returns to background levels by 56 ka. This peak may be related to the much lower amplitude features in the organic carbon flux and opal flux records 65–80 ka.

4. DISCUSSION

4.1. Precipitation and preservation of authigenic uranium

In oxygen-rich seawater, hexavalent uranium forms a highly soluble carbonate species $[UO_2(CO_3)_3]^{4-}$ (Langmuir, 1978) that imparts conservative behavior such that dissolved uranium concentrations scale with salinity in the water column (Owens et al., 2011). Within oxygenated porewaters, dissolved uranium maintains relatively high concentrations, but if the oxygen pool within the sediment pile becomes depleted, e.g. by benthic respiration, soluble U(VI) reduces to insoluble U(IV) and precipitates as solid UO_2 (Anderson, 1982; Anderson et al., 1989a; Morford and Emerson, 1999). This uranium reduction requires exceptionally low oxygen concentrations, equivalent to those required for iron reduction, Fe(III) to Fe(II) (Barnes and Cochran, 1990; Crusius et al., 1996; Zheng et al., 2002a), or the even lower oxygen conditions of sulfate reduction, S(VI) to S(-II) (Klinkhammer and Palmer, 1991). Dissimilatory iron-reducing microorganisms such as *Clostridium sp., Desulfovibrio sp.,* and *Shewanella sp.* likely facilitate the formation of reduced uranium precipitates by utilizing dissolved uranium as an electron acceptor to fuel their chemolithotrophic growth (Francis et al., 1994; Ganesh et al., 1997; Lovley et al., 1991; Sani et al., 2004). Although abiotic surface-catalyzation of uranium reduction is also possible (Kochenov et al., 1977; Liger et al., 1999; Nakashima et al., 1984), the low temperature sedimentary conditions are suboptimal for kinetically relevant inorganic uranium reduction compared to biologically mediated uranium reduction (Anderson et al., 1989a, 1989b; Cochran et al., 1986; Lovley et al., 1991; Tribovillard et al., 2006). Once uranium reduction commences, a steep uranium concentration gradient forms in the porewater along which additional soluble U(VI) will diffuse from the water column to support continued precipitation of authigenic U (aU) in the low oxygen zone (Anderson, 1982; Anderson et al., 1989b; Barnes and Cochran, 1990; Klinkhammer and Palmer, 1991). This diffusion-dependent, but otherwise unlimited, uranium source can thus create sedimentary aU peaks substantially enriched over U concentrations typically found in biogenic or lithogenic phases.

The disparate records of aU concentration from the six different cores (Fig. 3) most likely reflect the secondary effects of diagenesis on the preservation of aU in the sediment (Fig. 7). While the reduction of U occurs slowly without biological mediation, the kinetics of aU oxidation from U(IV) back to soluble U(VI) appear to be quite fast (Anderson et al., 1989a; Cochran et al., 1986), creating the phenomenon known as "burndown" (Jung et al., 1997; Mangini et al., 2001). If oxygen returns after some transient hypoxic period of aU deposition, that oxygen will diffuse into the sediment, oxidize uranium, and mobilize it into porewaters (McManus et al., 2005). Redissolution of U into porewaters reverses the concentration gradient with the overlying bottom waters so that U diffuses upwards and escapes into the water column (Mangini et al., 2001; Zheng et al., 2002b). Fluxes of U out of recently oxidized sediments have been observed in seasonally anoxic basins that experience cyclic aU deposition and reoxygenation (Anderson et al., 1989b; Cochran et al., 1986; Klinkhammer and Palmer, 1991; McManus et al., 2005; Zheng et al., 2002b). The loss of aU back to porewater may compromise sedimentary records of aU as a complete history of redox conditions (Mangini et al., 2001; McManus et al., 2005). If the aU is completely remobilized, its sedimentary record is eliminated entirely. For example, it is possible that aU precipitated in cores 05PC, 12PC, 38PC, and 39BB during MIS5, but subsequent reoxygenation of those sites obliterated the aU from their sedimentary records. Partial remobilization of aU may leave an aU record that does not extend as far in the sediment pile, as in 09PC relative to 35PC, and migration of U-rich porewater deeper in the sediment column can cause the precipitation of a secondary aU peak where the porewaters re-encounter reducing conditions (Mangini et al., 2001). This secondary peak may then stratigraphically pre-date the actual onset of reducing conditions (Jacobel et al., 2017;

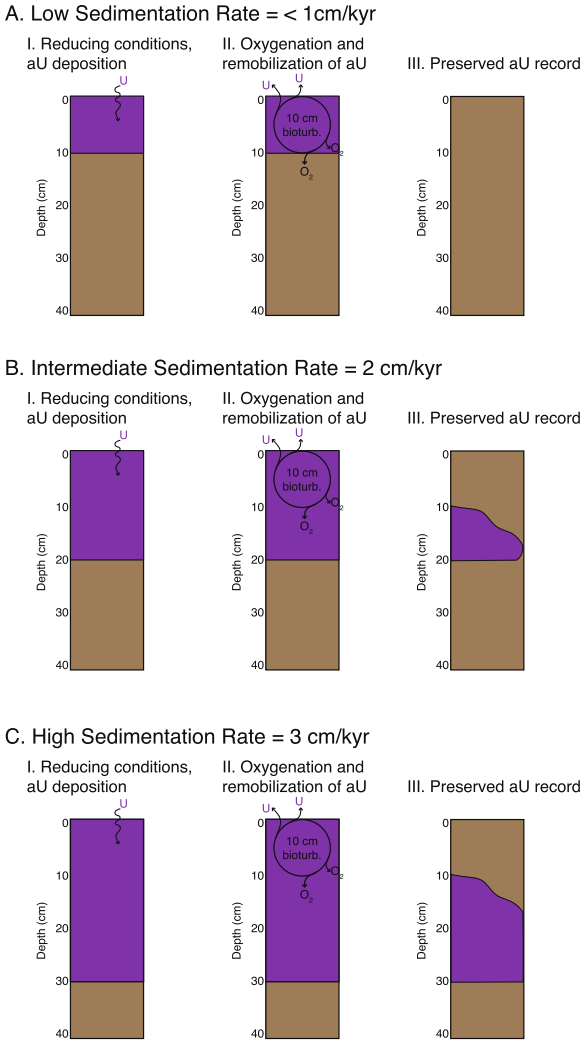

Fig. 7. Effect of burndown on aU preservation in sediments with varying sedimentation rates. I. All cores experience 10kyr of reducing conditions under which aU precipitates in the sediment. II. When oxygen subsequently returns to the sediment, bioturbation assists oxygen penetration down to 10 cm depth. In the presence of oxygen, aU remobilizes and diffuses out of the sediment. III. The preserved aU record depends on the sedimentation rate of the core. When sedimentation rates are low (A), no aU record may survive the re-oxygenation of the sediment pile. When sedimentation rates are higher (B and C), some aU is preserved in the sediment, but the record does not extend the full 10kyr duration of the reducing conditions.

Mills et al., 2010). These combined diagenetic effects suggest that relict aU peaks found in sedimentary records may be skewed towards lower amplitude, shorter duration, and earlier timing than the reducing conditions existed (Morford et al., 2009).

The extent to which burndown will alter the sedimentary aU record depends on both the organic carbon content (Mangini et al., 2001) and the sedimentation rate (Elderfield, 1985). Respiration of organic carbon in sediment consumes pore water oxygen and thus inhibits its availability to remobilize aU. Because higher organic carbon contents contribute to maintaining low oxygen conditions in the sediment, more intense burndown of aU will occur in sediments with low organic carbon fluxes (Jung et al., 1997; Mangini et al., 2001). The Juan de Fuca cores, however, are all proximal to one another (<30 km), and so variability in organic carbon delivery to the sediment is unlikely to explain the different degrees of burndown experienced amongst the six cores. Instead, they are subject to rates of burndown that are most likely determined by their highly variable sedimentation rates (Costa et al., 2016).

Low-sedimentation-rate sites are susceptible to complete redissolution of aU because their sedimentary aU pile will be relatively thin (Fig. 7A). After 10kyr of reducing conditions, a sediment core with 1 cm/kyr sedimentation rate will only contain 10 cm of sediment with elevated aU. When bottom waters reoxygenate, bioturbation may pump the oxygen-rich water through the mixed layer (10 cm, in this example) and facilitate aU oxidation and diffusion out of the sediment (McManus et al., 2005; Morford et al., 2009; Shimmield and Price, 1986; Zheng et al., 2002b). When sedimentation rates are higher (Fig. 7B and C), some of the aU is buried deep enough to be protected from oxygen exposure, but the duration of the preserved aU record is still shorter (5 kyr or 6.7 kyr) than the actual reducing conditions persisted (10 kyr). Previous studies have suggested that authigenic U preservation is compromised at sedimentation rates less than 2 cm/kyr (Mangini et al., 2001), and indeed, substantial aU burial on the JdFR only seems to occur when sedimentation rates are higher than 2 cm/kyr (Fig. 3B). The proximity of the six cores suggests that any change in redox conditions should be coincidentally observed in all six cores, but only the two cores with high sedimentation rates (≥3 cm/kyr) retain an aU signal during, e.g., MIS5. The older interglacial aU peak (MIS7) is only observed in 35PC, which maintains a sedimentation rate >2 cm/kyr in these intervals while even 09PC does not have high enough sedimentation rates to retain aU. The anomalous glacial peak (MIS8), also in 35PC, may be an artifact of the turbidite at 272 ka (Costa et al., 2016), which deposited 10 s of centimeters of sediment nearly instantaneously and thus cut off the porewater exchange with the overlying water column. Overall, it is likely that all six cores experienced high aU deposition during interglacial periods, but subsequent reoxygenation combined with intense bioturbation (10–15 cm, Costa et al., 2017b) removed the aU records from the slow-accumulating cores (05PC, 12PC, 38PC, 39BB). Thus, while the presence of aU is a good indicator for low-oxygen conditions, the absence of aU does not necessarily equate with persistent high-oxygen conditions.

4.2. Other trace metal (Mn, Ni, Zn, V) evidence for redox changes over time

While aU can provide an excellent redox history, sedimentation rates across much of the ocean, and particularly in the Pacific, fall below the 2 cm/kyr threshold for diagenetic resilience. In these regions, other redox-sensitive metals can be combined with aU to constrain the variability in sedimentary oxygen concentrations over time. We investi-

gate the utility of Mn, Zn, Ni, and V, all of which can be analyzed by high-resolution core-scanning XRF, as candidates for fast, accessible, and low-cost redox indicators in the near ridge sedimentary environment. Detailed trace metal behavior in sediments has been previously reviewed (e.g., Morford and Emerson, 1999; Schaller et al., 2000; Tribovillard et al., 2006; Morford et al., 2009; Mills et al., 2010), so only a synopsis of the relevant elements is included here.

4.2.1. Manganese

Mn is a major component of hydrothermal discharge, and most hydrothermal manganese in a plume is present in the dissolved form: >75% near the vent and ~50% in the plume on the EPR (Fitzsimmons et al., 2017) and generally >50% on the JdFR (Feely et al., 1994; Seyfried et al., 2003; Zheng et al., 2017). Oxidation of Mn occurs slowly via microbial catalyzation (Cowen et al., 1986; Dick et al., 2009; Tebo et al., 2004), and hydrothermal Mn is generally deposited to the underlying sediments as oxyhydroxide particles rather than as sulfides (Von Damm et al., 1998, 1985). Under changing redox conditions, sedimentary Mn responds in stark contrast to U. Mn solubility increases when it is reduced from Mn(IV) to Mn(II) (Froelich et al., 1979), so that it will mobilize out of sediment at the same time that aU is precipitating (Burdige and Gieskes, 1983; Lynn and Bonatti, 1965). Mn(II) does not substantially complex with organic matter or sulfides (Huerta-Diaz and Morse, 1992; Middelburg et al., 1987; Tribovillard et al., 2006) and only marginally reacts with carbonate (Boyle, 1983; Pedersen and Price, 1982). Sediments under reducing, noneuxinic conditions easily become depleted in Mn as it freely diffuses upward and escapes to the water column (e.g., Scholz et al., 2013; Shimmield and Price, 1986). Alternatively, when the oxygen pool within the sediment pile is high, particulate Mn oxy-hydroxides will be retained with the sediment while aU is mobilizing out of the sediment. Thus, redox driven diagenesis should result in anti-correlated Mn and aU profiles in sedimentary records, and coupling of these two redox indicators is a strategy often employed in pelagic sediment in which aU records are suspected to be influenced by preservation artifacts (e.g., Mangini et al., 2001; Morford et al., 2009).

The contrasting behavior of Mn and aU is apparent on the Juan de Fuca Ridge (Fig. 4 and Supplementary Table S2). Where aU concentrations are high (last interglacial, MIS5), Mn_{xs} fluxes are at their lowest (less than 4 mg/cm^2 kyr). Where aU concentrations are low (glacial periods, MIS2-4 and MIS6), Mn_{xs} fluxes are high, greater than 5 mg/cm^2 kyr and spiking at as much as 25 mg/cm^2 kyr. These trends in aU and Mn_{xs} fluxes are demonstrated by the extreme division (anti-correlation) between aU and Mn_{xs} fluxes (Fig. 5). Lower than average burial of hydrothermal Mn during interglacial periods suggests irreversible loss of Mn through diffusion back to the water column under reducing conditions. Excess burial during glacial periods may indicate precipitation of dissolved Mn out of seawater, possible due to the greater reservoir of dissolved hydrothermal Mn than other dissolved hydrothermal metals (Butterfield et al., 1997; Massoth et al., 1994). We therefore interpret high Mn_{xs} fluxes as strong evidence for oxidizing conditions.

4.2.2. Nickel

In the typical pelagic sediments of the abyssal ocean, sedimentary Ni concentrations are generally low (20 ppm in upper continental crust, Taylor and McClennan, 1995) and often not reported (or perhaps, not analyzed). Ni is not particularly soluble, and it is primarily sourced from deposition of lithogenic material, with additional contributions from organic matter in regions like continental margins with high organic fluxes (Calvert and Pedersen, 1993; Westerlund et al., 1986). In the near-ridge environment, sedimentary Ni concentrations are elevated due to scavenging of Ni from seawater by Fe oxyhydroxides (Dunk and Mills, 2006; Ford et al., 1999) and/or Mn oxyhydroxides (Kuhn et al., 2000; Metz et al., 1988). Increasing particulate Ni concentrations with increasing distance from the source vent are consistent with a hydrogenous rather than hydrothermal source of Ni (Dymond, 1981; Metz et al., 1988). This affiliation with hydrothermal particles increases the sedimentary inventory of Ni, which can subsequently be redistributed as a result of changing redox conditions.

Ni only has one prevalent oxidation state, Ni(II), and so its behavior in response to changing redox conditions is not geochemically inherent. Empirical evidence suggests that Ni remobilization may be largely controlled by co-precipitation and adsorption processes associated with the redox cycling of Mn (Dunk and Mills, 2006; Elderfield, 1985; Muñoz et al., 2012; Tribovillard et al., 2006). This affiliation between Ni and Mn is also observed on the Juan de Fuca Ridge (Figs. 4 and 5): high Ni_{xs} fluxes occur simultaneously with high Mn_{xs} fluxes during the last two glacial periods (MIS2-4, MIS6), and low Ni_{xs} fluxes (below 100 μg/cm^2 kyr) coincide with low Mn_{xs} fluxes (and high aU) during the last interglacial (MIS5). This correspondence suggests that Ni is predominantly associated with Mn oxides (as on the East Pacific Rise, Dunk and Mills, 2006), and that when Mn remobilizes in the sediment under reducing conditions, so does Ni (Feely et al., 1994; Santos-Echeandia et al., 2009; Shaw et al., 1990). The correlation between Ni and Mn appears weaker in older periods, particularly in MIS7 where low Mn_{xs} fluxes seem to coincide with slightly elevated Ni_{xs} fluxes and elevated aU fluxes. This behavior may indicate that complexation with organic matter (Calvert and Pedersen, 1993; Elderfield, 1981; Olson et al., 2017; Westerlund et al., 1986) or incorporation into relatively insoluble sulfides (Dyrssen and Kremling, 1990; Huerta-Diaz and Morse, 1992) may influence the redox distribution of Ni independently of Mn. However, the dominant redox mobilization of Ni appears to be in affiliation with Mn, and so we cautiously interpret high Ni_{xs} fluxes as evidence for oxidizing conditions.

4.2.3. Zinc

Unlike Mn or Ni, the primary source of Zn in the near ridge environment is hydrothermal sulfides, which precipitate in the buoyant plume shortly after being emitted from the vent (Edmonds and German, 2004; Feely et al., 1994; Findlay et al., 2015; German et al., 1991). Close to the vent,

80–90% of the emitted Zn is precipitated (German et al., 2002), primarily into sphalerite rather than pyrite or chalcopyrite (Findlay et al., 2015), but Fe may dope the sphalerite or circumprecipitate as an iron sulfide around the existing zinc sulfides (Findlay et al., 2015; Koski et al., 1994; Scott, 1983). The remaining 10–20% of emitted hydrothermal Zn may be scavenged by iron oxyhydroxides (German et al., 2002, 1991; Trocine and Trefry, 1988), stabilized as a dissolved species by chloro-complexation (Seewald and Seyfried, 1990; Trefry et al., 1994; Von Damm and Bischoff, 1987), or complexed with organic matter (Little et al., 2015). Dissolved Zn has been observed over 4000 km away from its hydrothermal origin (Roshan et al., 2016), but particulate Zn/Fe ratios in the plume decrease as the plume ages, likely due to Zn redissolving or settling out faster than Fe (Feely et al., 1994; Roshan et al., 2016; Trocine and Trefry, 1988).

Once deposited in the sediment, Zn is likely to be most mobile under oxidizing conditions that are corrosive to hydrothermal sulfides. Like Ni, Zn only has one oxidation state, Zn(II), and its redox sensitivity is largely controlled by its chemical environment. When sulfides are oxidized to sulfates, Zn will be released to porewaters where it can migrate out of the sediment, thus creating low Zn concentrations under high oxygen conditions. This result is similar to that observed in aU, and indeed Zn_{xs} fluxes show the same basic patterns as aU fluxes ($r^2 = 0.47$, Figs. 4 and 5). High Zn_{xs} fluxes (greater than 120 μg/cm^2 kyr) occur during the last interglacial periods (MIS5), with several cores recording a peak at 110 ka coincident with the aU peak. At the same time, there appears to be a component of the Zn_{xs} fluxes that is correlated with Mn_{xs} fluxes, despite the poor overall correlation ($r^2 = 0.17$). This Mn-driven redox behavior is particularly evident in 09PC in the last 60kyr, during which Zn_{xs} fluxes remain relatively high (>80 μg/cm^2 kyr) despite aU fluxes returning to background levels. This behavior may reflect limited diffusion of dissolved Zn in porewaters, such that the mobilized Zn during high oxygen periods may not have been able to escape the sediment pile at high accumulation rate sites (like 09PC). Alternatively, if sphalerite is only a small proportion of the total sulfide population, then Zn_{xs} fluxes may be influenced by sulfide capture (Huerta-Diaz and Morse, 1992), in which mobile Zn within porewaters can be pyritized by free sulfide ions released from other sulfide species. Overall the correlation between aU and Zn_{xs} fluxes suggests a primary sensitivity to reducing conditions, and so we tentatively interpret high Zn_{xs} fluxes as evidence for reducing conditions.

4.2.4. Vanadium

V, like Ni, is a hydrogenous metal that is scavenged from the water column by hydrothermal particulates, primarily iron oxyhydroxides (Morford and Emerson, 1999; Rudnicki and Elderfield, 1993; Schaller et al., 2000; Trocine and Trefry, 1988). Because seawater V concentrations are relatively low, sedimentary V concentrations due to scavenging tend to have low signal to noise ratios that can be difficult to identify and interpret. In the near ridge environment, high fluxes of hydrothermal iron may supply sufficient V that subsequent redox redistribution within the sedimentary pile can be distinguished. V becomes less soluble when it is reduced from V(V) to V(IV) (Calvert and Pedersen, 1993; Morford and Emerson, 1999), at which point it behaves like U (also IV in its reduced state), so that high sedimentary V_{xs} fluxes would be associated with low oxygen conditions. Furthermore, the redox threshold of V reduction is thought to be lower than that of Fe or Mn but higher than that of U (Morford and Emerson, 1999; Shaw et al., 1990), making it, theoretically, a sensitive indicator for the timing of redox transitions from aU precipitation to Mn retention. Indeed, on the Juan de Fuca Ridge, V_{xs} fluxes show the same basic patterns as Zn_{xs} and aU fluxes, with high V_{xs} fluxes during MIS5 and MIS7 coincident with peaks in aU (Fig. 4).

However, sedimentary V is often confounded by other processes that can affect both its delivery to the sediment and its response to changes in redox conditions. These complications are evident in the component of V_{xs} fluxes, mostly in 09PC, that is correlated with Mn_{xs} fluxes (Fig. 5). This component may reflect a susceptibility of V to Mn precipitation and dissolution cycles (Mills et al., 2010), such that V burial may actually be better preserved in oxic sediments than in anoxic sediments (Dunk and Mills, 2006). Furthermore, the efficiency of V scavenging from seawater is inversely dependent on phosphate concentrations (Edmonds and German, 2004; Feely et al., 1994), with which V competes for adsorption sites on iron oxyhydroxide particles (Dunk and Mills, 2006). Because phosphate is more readily scavenged than vanadate, higher phosphate concentrations may result in lower particulate V/Fe within hydrothermal plumes (Edmonds and German, 2004; Feely et al., 1994). A consequence of this exchange is that sedimentary V_{xs} fluxes may be recording changes in deep water nutrient concentrations rather than sediment redox variability. These factors all complicate the straightforward interpretation of V as a redox proxy, but its relationship with aU suggests that there is a redox signal also playing a role in V_{xs} fluxes. We therefore tentatively include V_{xs} fluxes in our redox reconstructions, with high V_{xs} fluxes as possible evidence for reducing conditions.

4.3. Relative Redox Potential (RRP) over the past 250 kyr

Because redox reactions proceed too slowly to achieve thermodynamic equilibrium (Balzer, 1982; Lindberg and Runnells, 1984; Postma, 1993), it is nearly impossible to reconstruct a precise paleo-redox history in absolute oxygen concentrations. Instead, we combine the information from multiple redox-sensitive elements (Mn, Ni, Zn, V, aU) to create a probabilistic relative redox potential (RRP) on an arbitrary scale. This conservative approach, outlined below, accommodates the many uncertainties associated with paleo-redox reconstructions. For example, the mineralogy and complexation of each element, which can affect the desired redox state and the kinetics of reaction, are poorly constrained, and mineralogical analyses on existing sediment may not be able to diagnose initial compositions or the formation of diagenetic ghost phases (like pyrite) that may have subsequently redissolved (Yarincik et al.,

2000). We focus this calculation on the last 250 kyr, for which aU variability is present. As previously mentioned (Section 4.1), the absence of aU (i.e., older than 250 ka) may be a diagenetic artifact and should not be interpreted as reflecting continuous high oxygen conditions.

Relative Redox Potentials (RRPs) for each core were calculated by converting Mn_{xs}, Ni_{xs}, V_{xs}, Zn_{xs} and aU fluxes into binary presence/absence designations, weighting each element by the strength and direction of its redox indication, summing the five elements, and then averaging the data in 5kyr bins. Binary fluxes were assigned as follows: 0 for any flux below the mean for that element in that core, and 1 for any flux above that mean. To create an arbitrary scale in which positive values are more oxidizing and negative values are more reducing, the following weights were employed: Mn = 2 (strong evidence for high oxygen conditions), Ni = 1 (weak evidence for high oxygen conditions), Zn = −1 (weak evidence for low oxygen conditions), V = −1 (weak evidence for low oxygen conditions) and aU = −2 (strong evidence for low oxygen conditions). The goal is to weight the elemental evidence of which we are more confident in a redox interpretation (aU and Mn) over those that are more tentative (Zn, V, Ni). When summed within each core, the elements create a quantized RRP with possible values limited to integers between −4 and 3 (Fig. 8A). The six cores were then averaged (mean) within each 5kyr bin to generate a single (unquantized) regional RRP (Fig. 8B). The RRP results are not sensitive to the inclusion of any one specific element (Supplementary Fig. S3), and they are robust even in the low sedimentation rate cores with poor preservation of aU (Supplementary Fig. S4). The results are further corroborated by RRPs calculated with metal/Mn ratios (Supplementary Fig. S5) or metal concentrations on a carbonate free basis (Supplementary Figs. S6 and S7).

This analysis demonstrates that the metal depositional histories from all six cores are consistent with low sedimentary oxygen conditions during interglacial periods, particularly during 100–120 ka (MIS5) but also 200–250 ka (MIS7). The records do not extend sufficiently into the Holocene to be conclusive. Sedimentary oxygen levels are relatively high during the last glacial period as well during MIS6. In fact, sedimentary oxygen levels may peak during peak glacial conditions, ~135–140 ka and 20–25 ka. This finding of higher oxygen conditions during glacial periods contrasts with previous studies that have found evidence for lower oxygen concentrations during glacial periods in the Pacific (Jacobel et al., 2017; Korff et al., 2016; Mills et al., 2010). However, there are three different processes that can account for low sedimentary oxygen concentrations: (1) bottom water oxygen (2) organic matter deposition and (3) sulfide deposition. In the next section, we will explore the evidence for and against each of these as drivers of the redox history of the sediment on the JdFR.

4.4. Mechanisms for changing sediment oxygen concentrations over time

4.4.1. Bottom water oxygen concentrations

In modern Pacific overturning circulation, the northernmost extent of North Pacific Deep Water (NPDW) blankets the Juan de Fuca Ridge before it retroflects and travels southward at depths of 2.5–3.5 km (e.g., Schmitz, Jr., 1995; Macdonald et al., 2009). Last ventilated in the South-

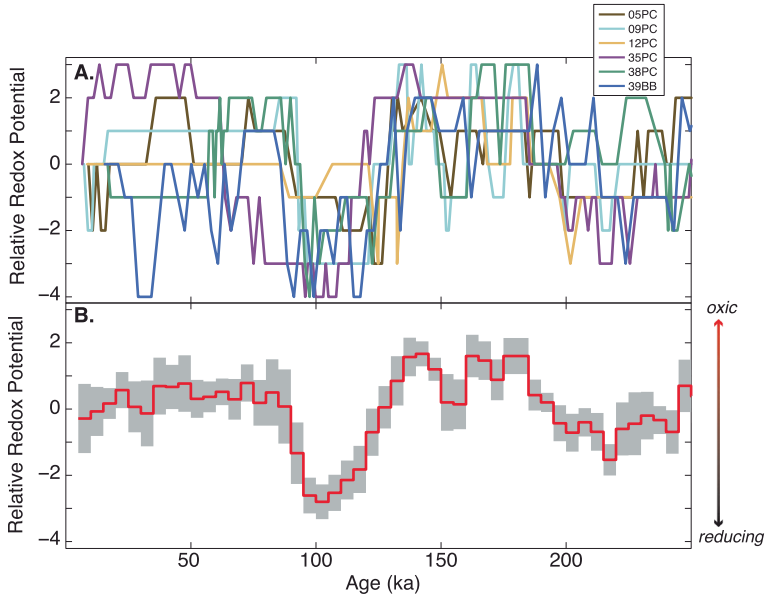

Fig. 8. Relative redox potentials (RRPs) for individual cores (A) and the regional mean (B) on the Juan de Fuca Ridge. RRPs are calculated by summing presence/absence records of each excess metal flux weighted by its relative redox indication (Mn = 2, Ni = 1, Zn = −1, V = −1, and U = −2). Individual records were calculated on a point-by-point basis by interpolating the excess metal fluxes onto the depths of the aU measurements. Individual records (A) were averaged (mean) within 5kyr bins to generate the regional mean signal in B. Each 5kyr bin is constrained by 11 datapoints, on average, and up to 45 datapoints. Positive values indicate more oxygen rich conditions.

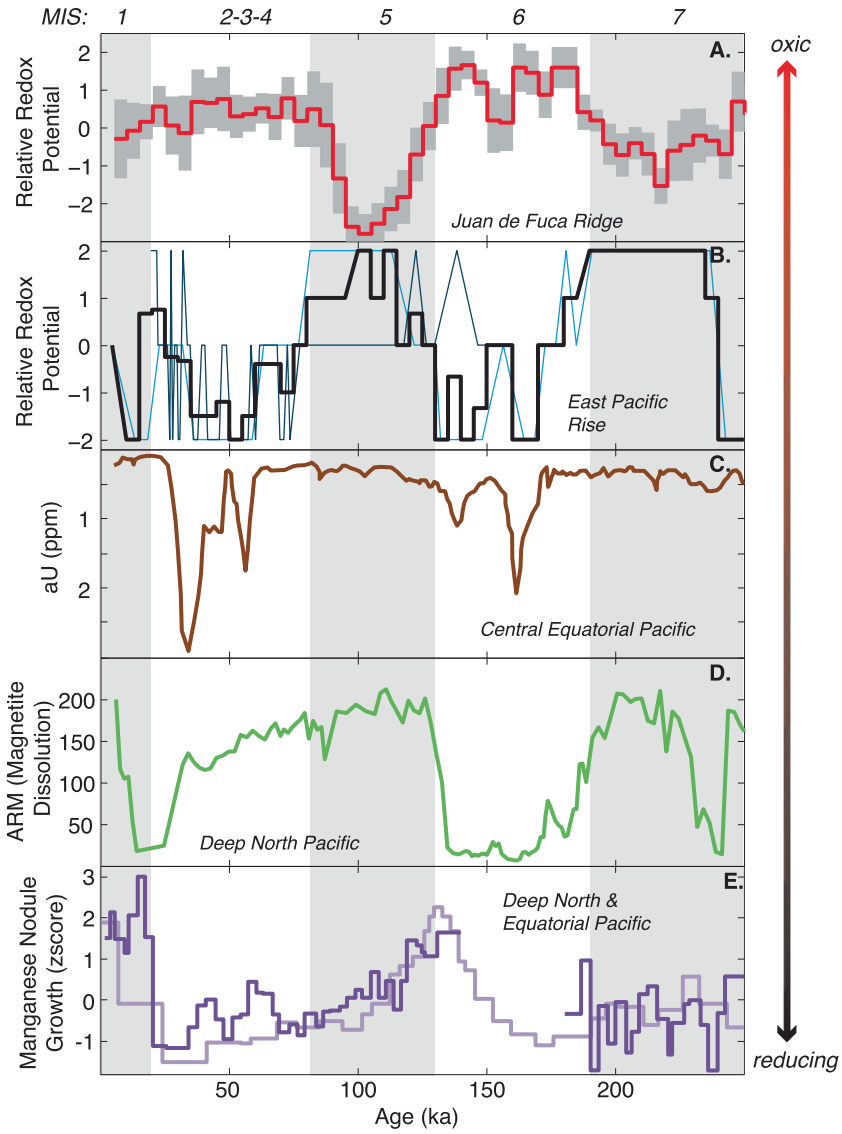

Fig. 9. Comparison of paleo-redox variability on the Juan de Fuca Ridge with other published redox records covering the last 250kyr in the Pacific. All records are oriented such that up indicates more oxygen rich conditions. A. RRP for the Juan de Fuca Ridge, as in Fig. 8. B. RRP for the East Pacific Rise, calculated as described in Section 4.3 using aU, Mn_{xs}, and V_{xa} fluxes from GS7202-35 (light blue) (Mills et al., 2010) and Y-71-7-53P (dark blue) (Lund et al., 2016; Schaller et al., 2000). Thick black line is the regional mean RRP of the two cores averaged (mean) within 5kyr bins. C. aU from Central Equatorial Pacific, ML1208-17PC (Jacobel et al., 2017). Metal concentrations in this carbonate-rich sediment core are too low to calculate RRPs. D. Anhysteretic remanent magnetization (ARM) from deep core SO202-1-39-3 (Korff et al., 2016). Low ARM indicates magnetite dissolution as a result of reducing conditions. E. Manganese nodule growth rates from two sites in the abyssal Pacific, 1550 m (light purple) and 4830 m (dark purple) (Mangini et al., 1990), normalized (zscore) to display on the same y-axis. Nodule growth depends on the flux of MnO_2, and so higher growth rates indicate periods of higher oxygen concentrations in the water column. Discontinuation of nodule growth 160–190 ka at the deeper site indicates particularly low oxygen concentrations compared to the shallower site during MIS6. (For interpretation of the references to colour in this figure legend, the reader is referred to the web version of this article.)

ern Ocean, this old and corrosive water mass has low oxygen concentrations due to the cumulative effect of respiration along its flowpath (Fig. 1) (Key et al., 2002; Kroopnick, 1985). Multiple lines of evidence, including sedimentological laminations, foraminiferal assemblages, magnetite dissolution, manganese nodule growth, trace metal deposition, and $\delta^{15}N$ diagenesis, have demonstrated that oxygen concentrations in Pacific deep waters (>2 km) were lower during the last glacial period (Fig. 9) (e.g., Bradtmiller et al., 2010; Galbraith et al., 2007; Galbraith and Jaccard, 2015; Jaccard and Galbraith, 2012; Jacobel et al., 2017; Korff et al., 2016; Mangini et al., 1990; Mills et al., 2010; Sigman and Boyle, 2000, and references there in). Glacial oxygen-depletion in deep waters was likely a consequence of increased stratification in the Southern Ocean (Anderson et al., 2009; Burke and Robinson, 2012;

Francois et al., 1997; Sigman and Boyle, 2000) as well as increased storage of respired carbon at depth (Anderson et al., 2014; Bradtmiller et al., 2010; Jaccard et al., 2016, 2009; Jacobel et al., 2017; Martinez-Garcia et al., 2014; Matsumoto et al., 2002). Therefore, any oxygen record capturing changes in NPDW would be expected to show lower oxygen concentrations during glacial periods.

The same would not necessarily be true for overlying intermediate waters (1–2 km). During the last glacial period, the upper ocean generally experienced better ventilation and higher oxygen concentrations than it does in interglacial periods (e.g., Duplessy et al., 1988; Jaccard and Galbraith, 2012; Poggemann et al., 2017; Sigman and Boyle, 2000; Stott et al., 2000). In the North Pacific, this water mass would be North Pacific Intermediate Water (NPIW), formed today in the Okhotsk Sea through cabbeling of the saline Kuroshio and the cold Oyashio current (You, 2003), an extrapolation of dense Okhotsk Sea Mode Water formed in the winter as a result of brine rejection (Talley, 1993). NPIW can easily be identified as a salinity minimum in the North Pacific (Keigwin, 1998), and this relatively low density ($\sigma = 26.8$) and steep halocline is what prevents true deep water formation and restricts NPIW to the upper water column (Emile-Geay et al., 2003; Warren, 1983). Oxygen concentrations in NPIW start out high near the formation zone but they are expended almost entirely en route to the California Margin (Bray, 1988). High intermediate water oxygen concentrations recorded on the California Margin during the last glacial period (Keigwin and Jones, 1990; Kennett and Ingram, 1995; Nameroff et al., 2004; Stott et al., 2000) are therefore a good indication that the NPIW, overall, was better ventilated.

Higher oxygen concentrations in NPIW could be generated if its glacial formation was more vigorous and/or more voluminous, both of which would aid oxygen retention as far east as the California Margin. Stronger NPIW formation has been modeled as a consequence of weakened AMOC (Max et al., 2017; Menviel et al., 2017; Okazaki et al., 2010), particularly during the last glacial termination. For example, during Heinrich Stadial 1 (17.5 ka), a near shutdown of AMOC (McManus et al., 2004) may have caused a pulse of NPIW formation that could account for transient ventilation peaks at that time (Mikolajewicz et al., 1997; Okazaki et al., 2010; Rae et al., 2014). Expectations for the production of NPIW during the glacial period itself would be much smaller, however, since the glacial-interglacial difference in AMOC vigor is relatively small compared to the changes during deglaciations (Böhm et al., 2015; Gherardi et al., 2009; McManus et al., 2004). Alternatively, enhanced NPIW formation during the glacial period might be a result of closure of the Bering Strait and new sources of NPIW formation in the Bering Sea (Horikawa et al., 2010; Knudson and Ravelo, 2015; Max et al., 2017).

Regardless of the mechanism driving NPIW formation, proxy evidence for the glacial expansion of a younger, better ventilated, lower nutrient water mass at intermediate water depths has been found not just near California but also elsewhere in the North Pacific. Glacial oxygenation is fairly well documented above 1.5 km (Jaccard and Galbraith, 2012), but the influence of NPIW below 2 km is still debated. Some proxy records propose that NPIW could not have penetrated below 2 km (Herguera et al., 2010; Keigwin, 1998; Matsumoto et al., 2002; Stott et al., 2000), while others have interpreted glacial NPIW signatures at 2.4 km depth (Gorbarenko, 1996), 2.6 km depth (Duplessy et al., 1988), and even 3.6 km during the deglaciation (Rae et al., 2014). Models have suggested that NPIW export may peak at 1.4 km (Menviel et al., 2017) but during deglaciation it may reach 2 km (Menviel et al., 2017) or 2.7 km (Okazaki et al., 2010). Similar patterns of manganese nodule growth at 1.55 km and 4.83 km water depth (Mangini et al., 1990) indicate similar changes in oxygen concentrations throughout the water column, and they suggest that any NPIW influence is limited to just the upper 1.5 km. As yet there is little proxy evidence or model simulations to support glacial NPIW reaching depths of 2.6–2.8 km, the depths of the Juan de Fuca Ridge cores, although data from this region are altogether sparse (Jaccard and Galbraith, 2012, see their Fig. 2). Glacial ventilation by NPIW would be consistent with increased oxygen concentrations reconstructed on the Juan de Fuca ridge in this study, but future work generating transects of ventilation from 2 to 3 km depth would be required to provide better constraints on the lower depth-limit of NPIW influence in the glacial North Pacific.

4.4.2. Organic matter delivery to the sediment

Organic matter is one of the strongest reducing agents available in the ocean. The aerobic respiration of organic matter can rapidly consume oxygen levels to the point of generating suboxic conditions and aU precipitation within the surface sediments (Anderson, 1982). Remineralization below high productivity regions can create oxygen deficient zones in the underlying water column (Key et al., 2002), and high fluxes of organic matter to the sediment can drive oxygen deficiency down into the sedimentary record. The extensive productivity peak during the Bolling-Allerod (~15 ka) in the North Pacific (Kohfeld and Chase, 2011) created locally hypoxic conditions observed in aU peaks (Lam et al., 2013), benthic foraminiferal assemblages (Praetorius et al., 2015), and sediment laminations (Davies et al., 2011). Besides this deglacial productivity peak, much of the North Pacific is characterized by lower productivity during glacial than during interglacial periods (e.g., Jaccard et al., 2005; Galbraith et al., 2007; Kohfeld and Chase, 2011). Biological growth during glacial periods may have been inhibited by both light limitation and prevention of upward mixing of deep nutrients due to enhanced surface stratification (Brunelle et al., 2010, 2007; Kienast et al., 2004; Ren et al., 2015; Sigman et al., 2004). If productivity was low during glacial periods and high during interglacial periods on the Juan de Fuca Ridge, then the cycles in organic fluxes to the sediment could generate the observed variability in RRP.

However, the three productivity proxies measured in this study each reconstructs a different productivity history, none of which would be consistent with the calculated RRP (Fig. 6). To attribute the reducing conditions in MIS5 to organic carbon fluxes, a particularly high flux of

organic carbon throughout the interglacial period would be expected. Instead, the organic carbon, opal, and Ba_{xs} fluxes record only transient features that suggest high productivity peaks during late deglaciation and early interglacial conditions. Other features in the productivity records, like the ~25 kyr cycles in organic carbon fluxes or the broad peak ~75 ka in Ba_{xs} fluxes, do not translate into similar features in the RRP. Overall, there appears to be very little evidence to definitively link the RRP to variability in organic matter.

Admittedly, this conclusion is dependent on taking the paleo-productivity proxies at face value, while the disagreement between them may instead indicate that they are imperfect records. The generally corrosive bottom waters combined with hydrothermal alteration of water column and sediment properties may create an environment simultaneously but variably harmful to the preservation of organic matter, opal, and Ba_{xs}. The nearly exponential decay in opal flux from the most recent period (0–20 ka, 22 mg/cm^2 kyr) to the oldest part of the record (200–250 ka, 5.3 mg/cm^2 kyr) suggests that opal, rather than being more robust than organic carbon to diagenesis, is in fact much more susceptible to post-depositional redissolution. Barite ($BaSO_4$) may be sensitive to changes in oxygen concentrations, in that intensive sulfate-reducing conditions, with substantial depletion of dissolved sulfate in pore waters, would reduce the preservation of Ba_{xs} and its utility as a productivity proxy (Torres et al., 1996; van Os et al., 1991). Within these limitations, however, there does not appear to be any conclusive evidence indicating that fluxes of organic matter have had a large influence on redox conditions. Future work using paleo-productivity proxies that are less susceptible to preservation issues, like Pa/Th, may help to provide more robust support for this conclusion.

4.4.3. Sulfide deposition due to hydrothermal activity

Instead of organic matter, another source of electron donors near mid-ocean ridges may be hydrothermal sulfides (Mills et al., 2010). Sediments near hydrothermal vents often contain concentrated aU deposits (>10 ppm) (Mills et al., 1993, 1994; Mills and Dunk, 2010; Schaller et al., 2000; Shimmield and Price, 1988) that have been ascribed to (1) deposition and subsequent oxidation of hydrothermal sulfides and/or (2) scavenging of U from seawater by settling hydrothermal particles. Elevated U/Fe ratios (~4 ppm/wt%) have been observed in suspended particles up to 200 m from the hydrothermal vents on the EPR (German et al., 2002) but they rapidly decline to negligible U enrichment (U/Fe $\leq$ 0.02 ppm/wt%) by 1.2 km from the ridge (Edmonds and German, 2004; German et al., 1991). Thus scavenging of U from seawater is not likely to be an important U delivery mechanism to sediment on the ridge flanks (e.g., >10 km from the ridge), and elevated U concentrations in sedimentary records (Metz et al., 1988; Mills et al., 1994; Sani et al., 2004; Shimmield and Price, 1988) must be generated by some in-situ process. Oxidation of sulfide minerals to soluble sulfates may be coupled to uranium reduction, in which U(VI) acts as the electron acceptor (Klinkhammer and Palmer, 1991; Langmuir, 1978; Wersin et al., 1994). Alternatively, oxidation of sulfide minerals may rapidly consume existing oxygen such that the benthic microbial assemblage shifts towards anaerobic microbes, including those that reduce uranium (see Section 4.1), so that sulfide oxidation and uranium reduction occur in rapid succession rather than coincidentally. The possible coupling between U and sulfide would produce a causal relationship between increased hydrothermal activity and more reducing conditions in the sediment.

Extensive study of hydrothermal deposits on the East Pacific Rise supports the hypothesis that the supply of hydrothermal sulfides is a major control on redox conditions in the sediment (Dunk and Mills, 2006; Mills et al., 2010; Mills and Dunk, 2010). If this is also the case on the Juan de Fuca Ridge, then interglacial reducing conditions may be a result of relatively higher hydrothermal activity at that time. Reconstructions based on hydrothermal Fe fluxes indicate high overall hydrothermal deposition during the last interglacial period, with two elevated peaks at 83 ka and 129 ka (Costa et al., 2017c). This pattern is broadly consistent with the RRP showing lower sedimentary oxygen concentrations during the last interglacial period (Fig. 8). Although the RRP does not capture the millennial scale peaks in hydrothermal activity, this may be an artifact of the RRP compilation that smooths the records over 5kyr bins. Alternatively, sulfides supplied intermittently by hydrothermal plumes may drive reducing conditions in the sediments over much longer sustained periods, especially when bioturbation rates are high. The influence of sulfides on the RRP is further corroborated by high Zn_{xs} fluxes during the last interglacial period, since the main carrier phase of Zn is indeed sulfides (Section 4.4.3). Redox reactions proceed slowly, so a small fraction of sulfides may oxidize and trigger aU precipitation while a large fraction of sulfides (e.g., Zn-sulfides) remain unreacted. If sulfide deposition is indeed an important influence on redox conditions, then it may imply that metal depositional environments are the most reducing at the same time that metal inputs from hydrothermal activity are the highest. This conjunction could have the potential effect of moderating metal burial such that hydrothermal deposition reconstructed from redox-sensitive metals may be underestimated.

5. CONCLUSIONS

Sedimentary concentrations of trace metals (Mn, Ni, Zn, V) and authigenic U (aU) were used to reconstruct redox conditions over the past 250 ka on the Juan de Fuca Ridge. Mn and Ni are indicators for high sedimentary oxygen concentrations, while Zn, V, and aU are indicators for low sedimentary oxygen concentrations. In contrast to previous studies from across the North Pacific at other depths and locations, sediment redox conditions were relatively oxygen rich on the Juan de Fuca Ridge during glacial periods compared to interglacial periods. We do not find strong evidence to attribute the low sediment oxygen conditions to an enhanced local organic carbon flux to the sediments during interglacial periods, although each of the three paleoproductivity proxies may be compromised by poor preservation. Alternatively, higher oxygen concentrations on the Juan de Fuca Ridge may result from better ventilation dur-

ing glacial periods, possibly due to enhanced North Pacific Intermediate Water (NPIW) formation, although there is as yet little evidence that NPIW can penetrate so deep in the water column. Finally, increased delivery and oxidation of hydrothermal sulfides from the nearby ridge may have created locally low sedimentary oxygen conditions during interglacial periods as a result of enhanced hydrothermal activity. If sulfides are indeed the dominant influence on the sediment redox reconstruction on the Juan de Fuca Ridge, then changes in sedimentary oxygen concentrations will be independent of any changes that may be occurring in bottom water oxygen concentrations.

ACKNOWLEDGEMENTS

The authors thank E. Glinskis and T. Liu for assistance with organic carbon analyses. Reviews from Augusto Mangini, Axel Durand, and an anonymous reviewer contributed valuable feedback to this project. This research was funded by NSF-FESD-#1338832, and dedicated to Harry Elderfield, an inspiration to us all.

APPENDIX A. SUPPLEMENTARY MATERIAL

Supplementary data associated with this article can be found, in the online version, at https://doi.org/10.1016/j.gca.2018.02.016.

REFERENCES

Anderson R. F. (1982) Concentration, vertical flux, and remineralization of particulate uranium in seawater. *Geochim. Cosmochim. Acta* **46**, 1293–1299.

Anderson R. F., Ali S., Bradtmiller L., Nielson S. H. H., Fleisher M. Q., Anderson B. E. and Burckle L. H. (2009) Wind-driven upwelling in the Southern Ocean and the deglacial rise in atmospheric CO_2. *Science* **323**, 1443–1448.

Anderson R. F., Barker S., Fleisher M., Gersonde R., Goldstein S. L., Kuhn G., Mortyn P. G., Pahnke K., Sachs J. P., Anderson R. F., Goldstein S. L., Mortyn P. G. and Sachs J. P. (2014) Biological response to millennial variability of dust and nutrient supply in the Subantarctic South Atlantic Ocean. *Philos. Trans. R. Soc. London* **372**, 20130054.

Anderson R. F., Fleisher M. Q. and LeHuray A. P. (1989a) Concentration, oxidation state, and particulate flux of uranium in the Black Sea. *Geochim. Cosmochim. Acta* **53**, 2215–2224.

Anderson R. F., LeHuray A. P., Fleisher M. Q. and Murray J. W. (1989b) Uranium deposition in Saanich Inlet sediments. Vancouver Island. *Geochim. Cosmochim. Acta* **53**, 2205–2213.

Balzer W. (1982) On the distribution of iron and manganese at the sediment/water interface: thermodynamics versus kinetic control. *Geochim. Cosmochim. Acta* **46**, 1153–1161.

Barnes C. E. and Cochran J. K. (1990) Uranium removal in oceanic sediments and the oceanic U balance. *Earth Planet. Sci. Lett.* **97**, 94–101.

Böhm E., Lippold J., Gutjahr M., Frank M., Blaser P., Antz B., Fohlmeister J., Frank N., Andersen M. B. and Deininger M. (2015) Strong and deep Atlantic meridional overturning circulation during the last glacial cycle. *Nature* **517**, 73–76.

Boyle E. A. (1983) Manganese carbonate overgrowths on foraminifera tests. *Geochim. Cosmochim. Acta* **47**, 1815–1819.

Bradtmiller L. I., Anderson R. F., Sachs J. P. and Fleisher M. Q. (2010) A deeper respired carbon pool in the glacial equatorial Pacific Ocean. *Earth Planet. Sci. Lett.* **299**, 417–425.

Bray N. A. (1988) Thermohaline circulation in the Gulf of California. *J. Geophys. Res.* **93**, 4993–5020.

Broecker W. S. (1982) Glacial to interglacial changes in ocean chemistry. *Prog. Oceanogr.* **11**, 151–197.

Brunelle B. G., Sigman D. M., Cook M. S., Keigwin L. D., Haug G. H., Plessen B., Schettler G. and Jaccard S. L. (2007) Evidence from diatom-bound nitrogen isotopes for subarctic Pacific stratification during the last ice age and a link to North Pacific denitrification changes. *Paleoceanography* **22**, 1–17.

Brunelle B. G., Sigman D. M., Jaccard S. L., Keigwin L. D., Plessen B., Schettler G., Cook M. S. and Haug G. H. (2010) Glacial/interglacial changes in nutrient supply and stratification in the western subarctic North Pacific since the penultimate glacial maximum. *Quat. Sci. Rev.* **29**, 2579–2590.

Burdige D. J. and Gieskes J. M. (1983) A pore water/solid phase diagenetic model for manganese in marine sediments. *Am. J. Sci.* **283**, 29–47.

Burke A. and Robinson L. F. (2012) The southern ocean's role in carbon exchange during the last deglaciation. *Science* **335**, 557–561.

Butterfield D. A., Jonasson I. R., Massoth G. J., Feely R. A., Roe K. K., Embley R. E., Holden J. F., McDuff R. E., Lilley M. D. and Delaney J. R. (1997) Seafloor eruptions and evolution of hydrothermal fluid chemistry. *Philos. Trans. R. Soc. London* **355**, 369–386.

Calvert S. E. and Pedersen T. F. (1993) Geochemistry of recent oxic and anoxic sediments: implications for the geological record. *Mar. Geol.* **113**, 67–88.

Cochran J. K., Carey A. E., Sholkovitz E. R. and Surprenant L. D. (1986) The geochemistry of uranium and thorium in coastal marine sediments and sediment pore waters. *Geochim. Cosmochim. Acta* **50**, 663–680.

Costa K. M. and McManus J. F. (2017) Efficacy of 230Th normalization in sediments from the Juan de Fuca Ridge, northeast Pacific Ocean. *Geochim. Cosmochim. Acta* **197**, 215–225.

Costa K. M., McManus J. F. and Anderson R. F. (2017b) Radiocarbon and stable isotope evidence for changes in sediment mixing in the North Pacific over the Past 30 kyr. *Radiocarbon*, 1–23.

Costa K. M., McManus J. F., Boulahanis B., Carbotte S. M., Winckler G., Huybers P. and Langmuir C. H. (2016) Sedimentation, stratigraphy and physical properties of sediment on the Juan de Fuca Ridge. *Mar. Geol.* **380**, 163–173.

Costa K. M., McManus J. F., Middleton J. L., Langmuir C. H., Huybers P. J., Winckler G. and Mukhopadhyay S. (2017c) Hydrothermal deposition on the Juan de Fuca Ridge over multiple glacial-interglacial cycles. *Earth Planet. Sci. Lett.* **479**, 120–132.

Cowen J. P., Massoth G. J. and Baker E. T. (1986) Bacterial scavenging of Mn and Fe in a mid- to far-field hydrothermal particle plume. *Nature* **322**, 169–171.

Crusius J., Calve S., Pedersen T. and Sage D. (1996) Rhenium and molybdenum enrichments in sediments as indicators of oxic, suboxic and sulfidic conditions of deposition. *Earth Planet. Sci. Lett.* **145**, 65–78.

Crusius J., Pedersen T. F., Kienast S., Keigwin L. and Labeyrie L. (2004) Influence of northwest Pacific productivity on North Pacific Intermediate Water oxygen concentrations during the Bolling-Allerod interval (14.7-12.9 ka). *Geology* **32**, 633–636.

Davies M. H., Mix A. C., Stoner J. S., Addison J. A., Jaeger J., Finney B. and Wiest J. (2011) The deglacial transition on the southeastern Alaska Margin: Meltwater input, sea level rise,

marine productivity, and sedimentary anoxia. *Paleoceanography* **26**, 1–18.
Dick G. J., Clement B. G., Webb S. M., Fodrie F. J., Bargar J. R. and Tebo B. M. (2009) Enzymatic microbial Mn(II) oxidation and Mn biooxide production in the Guyamas Basin deep-sea hydrothermal plume. *Geochim. Cosmochim. Acta* **73**, 6517–6530.
Dunk R. M. and Mills R. A. (2006) The impact of oxic alteration on plume-derived transition metals in ridge flank sediments from the East Pacific Rise. *Mar. Geol.* **229**, 133–157.
Duplessy J. C., Shackleton N. J., Fairbanks R. G., Labeyrie L., Oppo D. W. and Kallel N. (1988) Deepwater source variations during the last climatic cycle and their impact on the global deepwater circulation. *Paleoceanography* **3**, 343–360.
Dymond J. (1981) Geochemistry of Nazca plate surface sediments: an evaluation of hydrothermal, biogenic, detrital, and hydrogenous sources. *Geol. Soc. Am. Bull.* **154**, 133–172.
Dyrssen D. and Kremling K. (1990) Increasing hydrogen sulfide concentration and trace metal behavior in the anoxic Baltic waters. *Mar. Chem.* **30**, 193–204.
Edmonds H. N. and German C. R. (2004) Particle geochemistry in the Rainbow hydrothermal plume. Mid-Atlantic Ridge. *Geochim. Cosmochim. Acta* **68**, 759–772.
Elderfield H. (1981) Metal-organic associations in interstitial waters of Narragansett bay sediments. *Am. J. Sci.* **281**, 1184–1196.
Elderfield H. (1985) Element cycling in bottom sediments. *Philos. Trans. Roy. Soc. London* **23**, 19–23.
Elderfield H., Greaves M. J., Rudnicki M. D. and Hydes D. J. (1993) Aluminum reactivity in hydrothermal plumes at the Mid-Atlantic Ridge. *J. Geophys. Res.* **98**, 9667–9670.
Emile-Geay J., Cane M. A., Naik N., Seager R., Clement A. C. and van Geen A. (2003) Warren revisited: Atmospheric freshwater fluxes and "Why is no deep water formed in the North Pacific". *J. Geophys. Res* **108**, 3178.
Feely R. A., Lewison M., Massoth G. J., Robert-Baldo G., Lavelle J. W., Byrne R. H., Von Damm K. L. and Curl, Jr., H. C. (1987) Composition and dissolution of black smoker particulates from active vents on the juan de fuca ridge. *J. Geophys. Res.* **92**, 11347–11363.
Feely R. A., Massoth G. J., Trefry J. H., Baker E. T., Paulson A. J. and Lebon G. T. (1994) Composition and sedimentation of hydrothermal plume particles from north Cleft segment, Juan de Fuca Ridge. *J. Geophys. Res.* **99**, 4985–5006.
Findlay A. J., Gartman A., Shaw T. J. and Luther G. W. (2015) Trace metal concentration and partitioning in the first 1.5 m of hydrothermal vent plumes along the Mid-Atlantic Ridge: TAG, Snakepit, and Rainbow. *Chem. Geol.* **412**, 117–131.
Fitzsimmons J. N., John S. G., Marsay C. M., Hoffman C. L., Nicholas S. L., Toner B. M., German C. R. and Sherrell R. M. (2017) Iron persistence in a distal hydrothermal plume supported by dissolved-particulate exchange. *Nat. Geosci.* **10**, 195–201.
Fleisher M. Q. and Anderson R. F. (2003) Assessing the collection efficiency of Ross Sea sediment traps using 230Th and 231Pa. *Deep Sea Res Part II Top. Stud. Oceanogr.* **50**, 693–712.
Ford R. G., Kemner K. M. and Bertsch P. M. (1999) Influence of sorbate-sorbent interactions on the crystallization kinetics of nickel- and lead-ferrihydrite coprecipitates. *Geochim. Cosmochim. Acta* **63**, 39–48.
Francis A. J., Dodge C. J., Lu F., Halada G. P. and Clayton C. R. (1994) XPS and XANES studies of uranium reduction by *Clostridium sp.*. *Environ. Sci. Technol.* **28**, 636–639.
Francois R., Altabet M. A., Yu E., Sigman D. M., Bacon M. P., Frank M., Bohrmann G., Bareille G., Labeyrie L. D. and Geosciences (1997) Contribution of Southern Ocean surface-water stratification to low atmospheric CO_2 concentrations during the last glacial period. *Nature* **389**, 929–936.
Froelich P. N., Klinkhammer G. P., Bender M. L., Luedtke N. A., Heath G. R., Cullen D., Dauphin P., Hammond D., Hartman B. and Maynard V. (1979) Early oxidation of organic matter in pelagic sediments of the eastern equatorial Atlantic: suboxic diagenesis. *Geochim. Cosmochim. Acta* **43**, 1075–1090.
Galbraith E. D. and Jaccard S. L. (2015) Deglacial weakening of the oceanic soft tissue pump: global constraints from sedimentary nitrogen isotopes and oxygenation proxies. *Quat. Sci. Rev.* **109**, 38–48.
Galbraith E. D., Jaccard S. L., Pedersen T. F., Sigman D. M., Haug G. H., Cook M., Southon J. R. and Francois R. (2007) Carbon dioxide release from the North Pacific abyss during the last deglaciation. *Nature* **449**, 890–893.
Ganesh R., Robinson K. G. and Reed G. D. (1997) Reduction of hexavalent uranium from organic complexes by sulfate- and iron-reducing bacteria. *App. Env. Microbiol.* **63**, 4385–4391.
Garcia, H. E., Locarnini, R. A., Boyer, T. P., Antonov, J. I., Baranova, O. K., Zweng, M. M., Reagan, J. R. and Johnson, D.R. (2014) World Ocean Atlas 2013, Volume 3: Dissolved Oxygen, Apparent Oxygen Utilization, and Oxygen Saturation. In NOAA Atlas NESDIS 75 (eds. S. Levitus and A. Mishonov). p. 25.
German C. R., Colley S., Palmer M. R., Khripounoff A. and Klinkhammer G. P. (2002) Hydrothermal plume-particle fluxes at 13 degrees N on the East Pacific Rise. *Deep. Res. Part I-Oceanographic Res. Pap.* **49**, 1921–1940.
German C. R., Fleer A. P., Bacon M. P. and Edmond J. M. (1991) Hydrothermal scavenging at the Mid-Atlantic Ridge : radionuclide distributions. *Earth Planet. Sci. Lett.* **105**, 170–181.
Gherardi J.-M., Labeyrie L., Nave S., Francois R., McManus J. F. and Cortijo E. (2009) Glacial-interglacial circulation changes inferred from 231 Pa/ 230 Th Sedimentary Record in the North Atlantic region. *Paleoceanography* **24**, PA2204.
Gorbarenko S. A. (1996) Stable isotope and lithologic evidence of late-glacial and Holocene oceanography of the northwestern pacific and its marginal seas. *Quat. Res.* **250**, 230–250.
Herguera J. C., Herbert T., Kashgarian M. and Charles C. (2010) Intermediate and deep water mass distribution in the Pacific during the Last Glacial Maximum inferred from oxygen and carbon stable isotopes. *Quat. Sci. Rev.* **29**, 1228–1245.
Horikawa K., Asahara Y., Yamamoto K. and Okazaki Y. (2010) Intermediate water formation in the Bering Sea during glacial periods: Evidence from neodymium isotope ratios. *Geology* **38**, 435–438.
Huerta-Diaz M. A. and Morse J. W. (1992) Pyritisation of trace metals in anoxic marine sediments. *Geochim. Cosmochim. Acta* **56**, 2681–2702.
Jaccard S. L. and Galbraith E. D. (2012) Large climate-driven changes of oceanic oxygen concentrations during the last deglaciation. *Nat. Geosci.* **5**, 151–156.
Jaccard S. L., Galbraith E. D., Martínez-Garcia A. and Anderson R. F. (2016) Covariation of abyssal Southern Ocean oxygenation and pCO_2 throughout the last ice age. *Nature* **530**, 207–210.
Jaccard S. L., Galbraith E. D., Sigman D. M., Haug G. H., Francois R., Pedersen T. F., Dulski P. and Thierstein H. R. (2009) Subarctic Pacific evidence for a glacial deepening of the oceanic respired carbon pool. *Earth Planet. Sci. Lett.* **277**, 156–165.
Jaccard S. L., Haug G. H., Sigman D. M., Pedersen T. F., Thierstein H. R. and Rohl U. (2005) Glacial/interglacial changes in subarctic North Pacific stratification. *Science* **308**, 1003–1006.

Jacobel A. W., McManus J. F., Anderson R. F. and Winckler G. (2017) Repeated storage of respired carbon in the equatorial Pacific Ocean over the last three glacial cycles. *Nat. Commun.* **8**.

Jung M., Ilmberger J., Mangini A. and Emeis K.-C. (1997) Why some Mediterranean sapropels survived burn-down (and others did not). *Mar. Geol.* **141**, 51–60.

Keigwin L. D. (1998) Glacial-age hydrography of the far northwest Pacific Ocean. *Paleoceanography* **13**, 323–339.

Keigwin L. D. and Jones G. A. (1990) Deglacial climatic oscillations in the Gulf of California. *Paleoceanography* **5**, 1009–1023.

Kennett J. P. and Ingram B. L. (1995) A 20,000 year record of ocean circulation and climate change from the Santa Barbara basin. *Nature* **377**, 510–514.

Key R. M., Quay P. D., Schlosser P., McNichol A., von Reden K., Schneider R. J., Elder K. L., Stuiver M. and Östlund H. G. (2002) WOCE radiocarbon IV: Pacific ocean results; P10, P13N, P14C, P18, P19 & S4P. *Radiocarbon* **44**, 239–392.

Kienast S. S., Hendy I. L., Crusius J., Pedersen T. F. and Calvert S. E. (2004) Export production in the subarctic North Pacific over the last 800 kyrs: No evidence for iron fertilization? *J. Oceanogr.* **60**, 189–203.

Klinkhammer G. P. and Palmer M. R. (1991) Uranium in the oceans: Where it goes and why. *Geochim. Cosmochim. Acta* **55**, 1799–1806.

Knudson K. P. and Ravelo A. C. (2015) North Pacific Intermediate Water circulation enhanced by the closure of the Bering Strait. *Paleoceanography* **30**, 1–18.

Kochenov A. V., Korloev K. G., Dubinchuk V. T. and Medvedev Y. L. (1977) Experimental data on the conditions of precipitation of uranium from aqueous solutions. *Geochemistry Int.* **14**, 82–87.

Kohfeld K. E. and Chase Z. (2011) Controls on deglacial changes in biogenic fluxes in the North Pacific Ocean. *Quat. Sci. Rev.* **30**, 3350–3363.

Korff L., von Dobeneck T., Frederichs T., Kasten S., Kuhn G., Gersonde R. and Diekmann B. (2016) Cyclic magnetite dissolution in Pleistocene sediments of the abyssal northwest Pacific Ocean: evidence for glacial oxygen depletion and carbon trapping. *Paleoceanography* **31**, 600–624.

Koski R. A., Jonasson I. R., Kadko D. C., Smith V. K. and Wong F. L. (1994) Compositions, growth mechanisms, and temporal relations of hydrothermal sulfide-sulfate-silica chimneys at the northern Cleft segment, Juan de Fuca Ridge. *J. Geophys. Res. Solid Earth* **99**, 4813–4832.

Kroopnick P. M. (1985) The distribution of 13C of CO2 in the world oceans. *Deep Sea Res.* **32**, 57–84.

Kuhn T., Burger H., Castradori D. and Halbach P. (2000) Volcanic and hydrothermal history of ridge segments near the Rodrigues Triple Junction (Central Indian Ocean) deduced from sediment geochemistry. *Mar. Geol.* **169**, 391–409.

Lam P. J., Robinson L. F., Blusztajn J., Li C., Cook M. S., McManus J. F. and Keigwin L. D. (2013) Transient stratification as the cause of the North Pacific productivity spike during deglaciation. *Nat. Geosci.* **6**, 622–626.

Langmuir D. (1978) Uranium solution-mineral equilibria at low temperatures with applications to sedimentary ore deposits. *Geochim. Cosmochim. Acta* **42**, 547–569.

Liger E., Charlet L. and Van Cappellen P. (1999) Surface catalysis of uranium (VI) reduction by iron (II). *Geochim. Cosmochim. Acta* **63**, 2939–2955.

Lindberg R. D. and Runnells D. D. (1984) Ground Water Redox Reactions: An Analysis of Equilibrium State Applied to Eh Measurements and Geochemical Modeling. *Science* **225**, 925–927.

Little S. H., Vance D., Lyons T. W. and McManus J. (2015) Controls on trace metal authigenic enrichment in reducing sediments: Insights from modern oxygen-deficient settings. *Am. J. Sci.* **315**, 77–119.

Lovley D. R., Phillips E. J. P., Gorby Y. A. and Landa E. R. (1991) Microbial reduction of Uranium. *Nature* **350**, 413–416.

Lund D. C., Asimow P. D., Farley K. A., Rooney T. O., Seeley E., Jackson E. W. and Durham Z. M. (2016) Enhanced East Pacific Rise hydrothermal activity during the last two glacial terminations. *Science* **351**, 478–482.

Lunel T., Rudnicki M. D., Elderfield H. and Hydes D. J. (1990) Aluminium as a depth-sensitive tracer of entrainment in submarine hydrothermal plumes. *Nature* **344**, 137–139.

Lynn D. C. and Bonatti E. (1965) Mobility of manganese in diagenesis of deep-sea sediments. *Mar. Geol.* **3**, 457–474.

Macdonald A. M., Mecking S., Robbins P. E., Toole J. M., Johnson G. C., Talley L., Cook M. and Wijffels S. E. (2009) The WOCE-era 3-D Pacific Ocean circulation and heat budget. *Prog. Oceanogr.* **82**, 281–325.

Mangini A., Eisenhauer A. and Walter P. (1990) Response of manganese in the ocean to the climatic cycles in the Quaternary. *Paleoceanography* **5**, 811–821.

Mangini A., Jung M. and Laukenmann S. (2001) What do we learn from peaks of uranium and of manganese in deep sea sediments? *Mar. Geol.* **177**, 63–78.

Martinez-Garcia A., Sigman D. M., Ren H., Anderson R. F., Straub M., Hodell D. a., Jaccard S. L., Eglinton T. I. and Haug G. H. (2014) Iron fertilization of the subantarctic ocean during the last ice age. *Science* **343**, 1347–1350.

Massoth G. J., Baker E. T., Lupton J. E., Feely R. A., Butterfield D. A., Von Damm K. L., Roe K. K. and Lebon G. T. (1994) Temporal and spatial variability of hydrothermal manganese and iron at Cleft segment, Juan de Fuca Ridge. *J. Geophys. Res.* **99**, 4905–4923.

Matsumoto K., Oba T., Lynch-Stieglitz J. and Yamamoto H. (2002) Interior hydrography and circulation of the glacial Pacific Ocean. *Quat. Sci. Rev.* **21**, 1693–1704.

Max L., Rippert N., Lembke-Jene L., Mackensen A., Nurnberg D. and Tiedemann R. (2017) Evidence for enhanced convection of North Pacific Intermediate Water to the low-latitude Pacific under glacial conditions. *Paleoceanography* **32**, 41–55.

McManus J., Berelson W. M., Klinkhammer G. P., Hammond D. E. and Holm C. (2005) Authigenic uranium: relationship to oxygen penetration depth and organic carbon rain. *Geochim. Cosmochim. Acta* **69**, 95–108.

McManus J. F., Francois R., Gherardi J.-M., Keigwin L. D. and Brown-Leger S. (2004) Collapse and rapid resumption of Atlantic meridional circulation linked to deglacial climate changes. *Nature* **428**, 834–837.

Menviel L., Yu J., Joos F., Mouchet A., Meissner K. J. and England M. H. (2017) Poorly ventilated deep ocean at the Last Glacial Maximum inferred from carbon isotopes A data-model comparison study. *Paleoceanography* **32**, 2–17.

Metz S., Trefry J. H. and Nelsen T. a. (1988) History and geochemistry of a metalliferous sediment core from the Mid-Atlantic Ridge at 26°N. *Geochim. Cosmochim. Acta* **52**, 2369–2378.

Middelburg J. J., de Lange G. J. and Van der weijden C. H. (1987) Manganese solubility control in marine pore waters. *Geochim. Cosmochim. Acta* **51**, 759–763.

Mikolajewicz U., Crowley T. J., Schiller A. and Voss R. (1997) Modelling teleconnections between the North Atlantic and North Pacific during the Younger Dryas. *Nature* **387**, 384–387.

Mills R. A. and Dunk R. M. (2010) Tracing low-temperature fluid flow on ridge flanks with sedimentary uranium distribution. *Geochem. Geophys. Geosystems* **11**, Q08009.

Mills R. A., Taylor S. L., Pälike H. and Thomson J. (2010) Hydrothermal sediments record changes in deep water oxygen content in the SE Pacific. *Paleoceanography* **25**, PA4226.

Mills R. A., Thomson J., Elderfield H., Hinton R. W. and Hyslop E. (1994) Uranium enrichment in metalliferous sediments from the Mid-Atlantic Ridge. *Earth Planet. Sci. Lett.* **124**, 35–47.

Mills R., Elderfield H. and Thomson J. (1993) A dual origin for the hydrothermal component in a metalliferous. *J. Geophys. Res.* **98**, 9671–9681.

Morford J. L. and Emerson S. (1999) The geochemistry of redox sensitive trace metals in sediments. *Geochim. Cosmochim. Acta* **63**, 1735–1750.

Morford J. L., Martin W. R. and Carney C. M. (2009) Uranium diagenesis in sediments underlying bottom waters with high oxygen content. *Geochim. Cosmochim. Acta* **73**, 2920–2937.

Mortlock R. A. and Froelich P. N. (1989) A simple method for the rapid determination of biogenic opal in pelagic marine sediments. *Deep Sea Res.* **36**, 1415–1426.

Muñoz P., Dezileau L., Cardenas L., Sellanes J., Lange C. B., Inostroza J., Muratli J. and Salamanca M. a. (2012) Geochemistry of trace metals in shelf sediments affected by seasonal and permanent low oxygen conditions off central Chile, SE Pacific (~36°S). *Cont. Shelf Res.* **33**, 51–68.

Murray R. W., Leinen M. and Isern A. R. (1993) Biogenic flux of Al to sediment in the central equatorial Pacific Ocean: evidence for increased productivity during glacial periods. *Paleoceanography* **8**, 651–670.

Murray, R. W., Miller, D. J. and Kryc, K. A., 2000. Analysis of Major and Trace Elements in Rocks, Sediments, and Interstitial Waters by Inductively Coupled Plasma-Atomic Emission Spectrometry (ICP-AES). ODP Tech. Note.

Nakashima S., Disnar J.-R., Perruchot A. and Trichet J. (1984) Experimental study of mechanisms of fixation and reduction of uranium by sedimentary organic matter under diagenetic or hydrothermal conditions. *Geochim. Cosmochim. Acta* **48**, 2321–2329.

Nameroff T. J., Calvert S. E. and Murray J. W. (2004) Glacial-interglacial variability in the eastern tropical North Pacific oxygen minimum zone recorded by redox-sensitive trace metals. *Paleoceanography* **19**, PA1010.

Okazaki Y., Timmermann A., Menviel L., Harada N., Abe-Ouchi A., Chikamoto M. O., Mouchet A. and Asahi H. (2010) Deepwater Formation in the North Pacific during the last glacial termination. *Science* **329**, 200–204.

Olson L., Quinn K. A., Siebecker M. G., Luther G. W., Hastings D. and Morford J. L. (2017) Trace metal diagenesis in sulfidic sediments: Insights from Chesapeake Bay. *Chem. Geol.* **452**, 47–59.

Owens S. A., Buesseler K. O. and Sims K. W. W. (2011) Re-evaluating the 238U-salinity relationship in seawater: Implications for the 238U–234Th disequilibrium method. *Mar. Chem.* **127**, 31–39.

Pedersen T. F. and Price N. B. (1982) The geochemistry of manganese carbonate in Panama Basin sediments. *Geochim. Cosmochim. Acta* **46**, 59–68.

Poggemann D., Hathorne E. C., Nürnberg D., Frank M., Bruhn I., Reißig S. and Bahr A. (2017) Rapid deglacial injection of nutrients into the tropical Atlantic via Antarctic Intermediate Water. *Earth Planet. Sci. Lett.* **463**, 118–126.

Postma D. (1993) The reactivity of iron oxides in sediments: A kinetic approach. *Geochim. Cosmochim. Acta* **57**, 5027–5034.

Praetorius S. K., Mix A. C., Walczak M. H., Wolhowe M. D., Addison J. A. and Prahl F. G. (2015) North Pacific deglacial hypoxic events linked to abrupt ocean warming. *Nature* **527**, 362–366.

Rae J. W. B., Sarnthein M., Foster G. L., Ridgewell A., Grootes P. M. and Elliott T. (2014) Deep water formation in the North Pacific and deglacial CO2 rise. *Paleoceanography* **29**, 645–667.

Ren H., Studer A. S., Serno S., Sigman D. M., Winckler G., Anderson R. F., Oleynik S., Gersonde R. and Haug G. H. (2015) Glacial-to-interglacial changes in nitrate supply and consumption in the subarctic North Pacific from microfossil-bound N isotopes at two trophic levels. *Paleoceanography* **30**, 1217–1232.

Resing J. A., Sedwick P. N., German C. R., Jenkins W. J., Moffett J. W., Sohst B. M. and Tagliabue A. (2015) Basin-scale transport of hydrothermal dissolved metals across the South Pacific Ocean. *Nature* **523**, 200–203.

Roshan S., Wu J. and Jenkins W. J. (2016) Long-range transport of hydrothermal dissolved Zn in the tropical South Pacific. *Mar. Chem.* **183**, 25–32.

Rudnicki M. D. and Elderfield H. (1993) A chemical model of the buoyant and neutrally buoyant plume above the TAG vent field, 26 degrees N Mid-Atlantic Ridge. *Geochim. Cosmochim. Acta* **57**, 2939–2957.

Sani R. K., Peyton B. M., Amonette J. E. and Geesey G. G. (2004) Reduction of uranium (VI) under sulfate-reducing conditions in the presence of Fe (III)-(hydr)oxides. *Geochim. Cosmochim. Acta* **68**, 2639–2648.

Santos-Echeandia J., Prego R., Cobelo-García A. and Millward G. E. (2009) Porewater geochemistry in a Galician Ria (NW Iberian Peninsula): Implications for benthic fl uxes of dissolved trace elements (Co, Cu, Ni, Pb, V, Zn). *Mar. Chem.* **117**, 77–87.

Schaller T., Morford J. L., Emerson S. and Feely R. A. (2000) Oxyanions in metalliferous sediments: tracers for paleoseawater metal concentrations? *Geochim. Cosmochim. Acta* **64**, 2243–2254.

Schmitz, Jr., W. J. (1995) On the interbasin-scale thermohaline circulation. *Rev. Geophys.* **33**, 151–173.

Scholz F., McManus J. and Sommer S. (2013) The manganese and iron shuttle in a modern euxinic basin and implications for molybdenum cycling at euxinic ocean margins. *Chem. Geol.* **355**, 56–68.

Scott S. D. (1983) Chemical behaviour of sphalerite and arsenopyrite in hydrothermal and metamorphic envirnments. *Mineral. Mag.* **47**, 427–435.

Seewald J. S. and Seyfried W. E. (1990) The effect of temperature on metal mobility in subseafloor hydrothermal systems: constrains from basalt alteration experiments. *Earth Planet. Sci. Lett.* **101**, 388–403.

Serno S., Winckler G., Anderson R. F., Maier E., Ren H., Gersonde R. and Haug G. H. (2015) Comparing dust flux records from the Subarctic North Pacific and Greenland: Implications for atmospheric transport to Greenland and for the application of dust as a chronostratigraphic tool. *Paleoceanography* **30**, 583–600.

Seyfried W. E., Seewald J. S., Berndt M. E., Ding K. and Foustoukos D. I. (2003) Chemistry of hydrothermal vent fluids from the Main Endeavour Field, northern Juan de Fuca Ridge: geochemical controls in the aftermath of June 1999 seismic events. *J. Geophys. Res.* **108**, 2429.

Shaw T. J., Gieskes J. M. and Jahnke R. A. (1990) Early diagenesis in differing depositional environments : The response of transition metals in pore water. *Geochim. Cosmochim. Acta* **54**, 1233–1246.

Shimmield G. B. and Price N. B. (1986) The behaviour of molybdenum and manganese during early sediment diagenesis – offshore Baja California, Mexico. *Mar. Chem.* **19**, 261–280.

Shimmield G. B. and Price N. B. (1988) The scavenging of U, 230Th, and 231Pa during pulsed hydrothermal activity at 20°S, East Pacific Rise. *Geochim. Cosmochim. Acta* **52**, 669–677.

Sigman D. M. and Boyle E. A. (2000) Glacial/interglacial variationsin atmospheric carbon dioxide. *Nature* **407**, 859–869.
Sigman D. M., Jaccard S. L. and Haug G. H. (2004) Polar ocean stratification in a cold climate. *Nature* **428**, 59–63.
Stott L. D., Neumann M. and Hammond D. (2000) Intermediate water ventilation on the northeastern Pacific margin during the late Pleistocene inferred from benthic foraminiferal $\delta^{13}C$. *Paleoceanography* **15**, 161–169.
Taguchi K. and Narita H. (1995) 230Th and 231Pa distributions in surface sediments off Enshunada, Ja. In *Biogeochemical Processes and Ocean Flux in the Western Pacific* (eds. H. Sakai and Y. Nozaki). Terra Scientific Publishing Company, Tokyo, pp. 375–382.
Talley L. D. (1993) Distribution and formation of North Pacific intermediate water. *Am. Meteorol. Soc.* **23**, 517–537.
Taylor S. R. and McLennan S. M. (1995) The geochemical evolution of the continental crust. *Rev. Geophys.* **33**, 241–265.
Tebo B. M., Bargar J. R., Clement B. G., Dick G. J., Murray K. J., Parker D., Verity R. and Webb S. M. (2004) Biogenic manganese oxides: properties and mechanisms of formation. *Annu. Rev. Earth Planet. Sci.* **32**, 287–328.
Torres M. E., Brumsack H. J., Bohrmann G. and Emeis K.-C. (1996) Barite fronts in continental margin sediments: a new look at barium remobilization in the zone of sulfate reduction and formation of heavy barites in diagenetic fronts. *Chem. Geol.* **127**, 125–139.
Trefry J. H., Butterfield D. B., Metz S., Massoth G. J., Trocine R. P. and Feely R. A. (1994) Trace metals in hydrothermal solution from Cleft segment on the southern Juan de Fuca Ridge. *J. Geophys. Res.* **99**, 4925–4935.
Tribovillard N., Algeo T. J., Lyons T. and Riboulleau A. (2006) Trace metals as paleoredox and paleoproductivity proxies: an update. *Chem. Geol.* **232**, 12–32.
Trocine R. P. and Trefry J. H. (1988) Distribution and chemistry of suspended particles from an active hydrothermal vent site on the Mid-Atlantic Ridge at 26°N. *Earth Planet. Sci. Lett.* **88**, 1–15.
van Os B. J., Middelburg J. J. and de Lange G. J. (1991) Possible diagenetic mobilization of barium in sapropelic sediment from the eastern Mediterranean. *Mar. Geol.* **100**, 125–136.
Von Damm K. L. and Bischoff J. L. (1987) Chemistry of hydrothermal solutions from the southern Juan de Fuca Ridge. *J. Geophys. Res.* **92**, 11334.
Von Damm K. L., Bray A. M., Buttermore L. G. and Oosting S. E. (1998) The geochemical controls on vent fluids from the Lucky Strike vent field Mid-Atlantic Ridge. *Earth Planet. Sci. Lett.* **160**, 521–536.
Von Damm K. L., Edmond J. M., Grant B., Measures C. I., Walden B. and Weiss R. F. (1985) Chemistry of submarine hydrothermal solutions at 21°N East Pacific Rise. *Geochim. Cosmochim. Acta* **49**, 2197–2220.
Warren B. A. (1983) Why is no deep water formed in the North Pacific? *J. Mar. Res.* **41**, 327–347.
Wersin P., Hochella, Jr., M. F., Persson P., Redden G., Leckie J. and Harris D. W. (1994) Interaction between aqueous uranium (VI) and sulfide minerals: Spectroscopic evidence for sorption and reduction. *Geochim. Cosmochim. Acta* **58**, 2829–2843.
Westerlund S. F. G., Anderson L. G., Hall P. O. J., Iverfeldt A., van der Loeff M. M. R. and Sundby B. (1986) Benthic fluxes of cadmium, copper, nickel, zinc, and lead in the coastal environment. *Geochim. Cosmochim. Acta* **50**, 1289–1296.
Yarincik K. M., Murray R. W., Lyons T. W., Peterson L. C. and Haug G. H. (2000) Oxygenation history of bottom waters in the Cariaco Basin, Venezuela, over the past 578,000 years: Results from redox-sensitive metals (Mo, V, Mn, and Fe). *Paleoceanography* **15**, 593–604.
You Y. (2003) Implications of cabbeling on the formation and transformation mechanism of North Pacific intermediate water. *J. Geophys. Res.* **108**, 1–24.
Zheng L., Minami T., Takano S. and Minami H. (2017) Distribution and stoichiometry of Al, Mn, Fe Co, Ni, Cu, Zn, Cd, and Pb in seawater around the Juan de Fuca Ridge. *J. Oceanogr.* **73**, 669–685.
Zheng Y., Anderson R. F., Van Geen A. and Fleisher M. Q. (2002a) Preservation of particulate non-lithogenic uranium in marine sediments. *Geochim. Cosmochim. Acta* **66**, 3085–3092.
Zheng Y., Anderson R. F., Van Geen A. and Fleisher M. Q. (2002b) Remobilization of authigenic uranium in marine sediments by bioturbation. *Geochim. Cosmochim. Acta* **66**, 1759–1772.

FURTHER READING

Costa, K. M., Jacobel, A. W., McManus, J. F., Anderson, R. F., Winckler, G. and Thiagarajan, N. (2017a) Productivity patterns in the Equatorial Pacific over the last 30,000 years. Global Biogeochem. Cycles 31.

Associate editor: Thomas M. Marchitto